IB-DNQ and Rucaparib dual treatment alters cell cycle regulation and DNA repair in triple negative breast cancer cells

Avery M. Runnebohm[1], H.R. Sagara Wijeratne[1], Sarah A. Peck Justice[1,2], Aruna B. Wijeratne[1,5], Gitanjali Roy[1], Naveen Singh[3], Paul Hergenrother[4], David A. Boothman[1,5], Edward A. Motea[1,5], Amber L. Mosley[1,5,6]

[1]*Department of Biochemistry and Molecular Biology, Indiana University School of Medicine, Indianapolis, IN*

[2]*Department of Biology, Marian University, Indianapolis, IN*

[3]*Charles River Laboratories, Spencerville, OH*

[4]*Department of Chemistry, University of Illinois Urbana-Champaign, Urbana, IL*

[5]*IU Simon Comprehensive Cancer Center, Indianapolis, IN*

[6]*Center for Computational Biology and Bioinformatics, Indiana University School of Medicine, Indianapolis, IN*

Corresponding author: Amber Mosley, almosley@iu.edu

ABSTRACT

Background: Triple negative breast cancer (TNBC), characterized by the lack of three canonical receptors, is unresponsive to commonly used hormonal therapies. One potential TNBC-specific therapeutic target is NQO1, as it is highly expressed in many TNBC patients and lowly expressed in non-cancer tissues. DNA damage induced by NQO1 bioactivatable drugs in combination with Rucaparib-mediated inhibition of PARP1-dependent DNA repair synergistically induces cell death.

Methods: To gain a better understanding of the mechanisms behind this synergistic effect, we used global proteomics, phosphoproteomics, and thermal proteome profiling to analyze changes in protein abundance, phosphorylation and protein thermal stability.

Results: Very few protein abundance changes resulted from single or dual agent treatment; however, protein phosphorylation and thermal stability were impacted. Histone H2AX was among several proteins identified to have increased phosphorylation when cells were treated with the combination of IB-DNQ and Rucaparib, validating that the drugs induced persistent DNA damage. Thermal proteome profiling revealed destabilization of H2AX following combination treatment, potentially a result of the increase in phosphorylation. Kinase substrate enrichment analysis predicted altered activity for kinases involved in DNA repair and cell cycle following dual agent treatment. Further biophysical analysis of these two processes revealed alterations in SWI/SNF complex association and tubulin / p53 interactions.

Conclusions: Our findings that the drugs target DNA repair and cell cycle regulation, canonical cancer treatment targets, in a way that is dependent on increased expression of a protein selectively found to be upregulated in cancers without impacting protein

abundance illustrate that multi-omics methodologies are important to gain a deeper understanding of the mechanisms behind treatment induced cancer cell death.

Key words:

Triple negative breast cancer, IB-DNQ, Rucaparib, multiomics, mass spectrometry, DNA damage, cell cycle

BACKGROUND

Triple negative breast cancer (TNBC) is a subset of breast cancer that accounts for 15-25% of cases (1). TNBC is more aggressive than most other breast cancer types, with approximately 46% of patients developing metastases and an average tumor recurrence of 1.2 years (1–3). TNBC is characterized by a lack of estrogen, progesterone, and human epidermal growth factor 2 receptors, which render these tumors unresponsive to commonly used hormonal therapies (4,5). Conventional treatments of TNBC include alkylating agents, anti-microtubule agents, anti-metabolites, and platinum (2). For advanced cases of TNBC, new immunotherapies have emerged, but even with these therapies, TNBC has a 5-year survival rate of 8-16% (2,3). An efficacious tumor type-specific treatment would greatly improve outcomes for patients with TNBC.

NAD(P)H:quinone oxidoreductase 1 (NQO1) bioactivatable agents have been shown previously to cause tumor-selective DNA damage and cell death (6,7). The NQO1 bioactivatable drug β-lapachone (ARQ761 in clinical form) has been tested in clinical

trials for patients with solid tumors with metastasis or that have recurrent or nonresectable tumors (8). However, two other NQO1 bioactivatable drugs, deoxynyboquinone (DNQ) and its derivative isobutyl deoxynyboquinone (IB-DNQ), have been shown to be more potent than β-lapachone in killing cancer cells (9,10). These drugs induce DNA damage and hyperactivation of the DNA repair enzyme PARP1, leading to reduction of essential nucleotides and programmed necrosis (11,12). These drugs are promising in the treatment of TNBC and other solid tumors with overexpression of NQO1 and an elevated NQO1:catalase expression ratio (13). Many solid tumors, including those from thyroid, adrenal, breast, ovarian, colon, cornea, and non-small cell lung cancer tissues, have significantly increased NQO1 expression compared to normal tissues (14). NQO1 is a quinone reductase that catalyzes two-electron reduction of quinones to hydroquinones using NADH or NADPH as electron donors (15,16). NQO1 bioactivatable drugs, including β-lapachone and IB-DNQ, undergo oxidoreduction by NQO1 which results in unstable hydroquinones that spontaneously convert back to the original compound (12) (Figure 1a). This NQO1-dependent futile redox cycling oxidizes NADPH to create reactive oxygen species (ROS), most of which are superoxide radicals (17). Superoxide dismutase converts superoxide radicals into oxygen and hydrogen peroxide, and catalase catalyzes degradation of hydrogen peroxide to protect cell from damage (reviewed in (18)). Treating tumors that highly express NQO1 and lowly express catalase with NQO1 bioactivatable drugs will lead to ROS induced-DNA damage specifically within the tumor cells, making these tumors ideal targets for NQO1 bioactivatable drugs. β-Lapachone

and IB-DNQ have potential to be used as single agent treatments, but strategies to improve efficacy while minimizing toxicity are needed.

DNA repair mechanisms have long been targets for cancer therapies (19,20). Poly(ADP-ribose) polymerase-1 (PARP1) is a poly-ADP-ribosyltransferase that mediates poly-ADP-ribosylation (PARylation) and plays an important role in multiple DNA repair pathways (21–23). PARP1 inhibitors, including Olaparib, Rucaparib, Niraparib, and Talazoparib, have been approved by the FDA for treatment of ovarian and breast cancers (21). Huang et al (2016) showed that pretreating NQO1+ TNBC cells with non-lethal concentration of Rucaparib, followed by co-treatment with β-lapachone leads to tumor-selective cell death (11). PARP1 becomes hyperactive following treatment with β-lapachone, where self PARylation (PAR-PARP1) inactivates the protein and prevents PARP1 from binding DNA and activating DNA repair processes (24,25). Therefore, inhibiting PARP1 with Rucaparib prior to β-lapachone exposure enhances NQO1-dependent DNA damage and apoptosis while lowering the efficacious dose of β-lapachone and decreasing toxicity (Figure 1b) (11).

The downstream mechanisms leading to tumor-selective cell death by dual agent treatment with NQO1 bioactivatable drugs and Rucaparib are not completely understood. Here we are using several proteomics techniques (e.g. global analysis, phosphoproteomics, and thermal proteome profiling) to gain a better understanding of the effects of IB-DNQ and Rucaparib on protein abundance, protein phosphorylation, and protein thermal stability (Figure 1c). We report that the dual agent treatment results

in significant changes in protein phosphorylation and thermal stability with minimal impacts on protein abundance. Deeper analysis into the proteins with changes in phosphorylation and / or thermal stability revealed alterations in DNA damage response and cell cycle regulation. Specifically, we observe changes in phosphorylation of H2AX and in protein-complex stability of chromatin remodeling machinery, indicative of accumulation of DNA damage. We also show significant changes in cell cycle kinase activity and protein thermal stability of several cell cycle regulators and DNA repair proteins. The synergistic effect of these two drugs is dependent on NQO1 expression, further supporting the tumor-specificity of this dual agent treatment. Tumor-specific targeting of two hallmark cancer targets, cell cycle regulation and DNA damage, by IB-DNQ and Rucaparib combination treatment provides strong support for their potential use as a clinical therapy for patients with TNBC.

RESULTS

Characterizing global protein and phosphorylation dynamics following IB-DNQ and Rucaparib treatment

Previous studies determined that dual treatment of lung, pancreas, and breast cancer cell types with low concentrations of β-lapachone and Rucaparib leads to increased cancer cell death compared to either treatment alone, indicating synergistic lethality (11). However, the effects of these drugs on protein abundance and function and the downstream mechanisms that lead to cell death have not been studied. We performed global proteomics using isogenic TNBC cell lines using MDA-MB-231 that contain a polymorphism in NQO1 that lead to its rapid degradation (NQO1*2), and NQO1+ cells

where wild-type NQO1 was stably overexpress by plasmid. These cell line models allowed us to gain an initial, broad understanding of the protein abundance changes occurring as a result of the drug treatments. Four biological replicates of each cell line were grown and treated with a sublethal low dose (0.1 µM) IB-DNQ, a lethal high dose (0.4 µM) IB-DNQ, 15 uM Rucaparib, or a combination of low dose IB-DNQ and Rucaparib for 2-4 hours (9,11). Cells were collected and lysed, and resulting global protein abundance was analyzed using LC-MS^2. A total of 8,070 proteins were identified across all treatment groups and genotypes. Overall, only 18 proteins had significant changes ($p \leq 0.05$) in abundance with the drug treatments compared to the control in NQO1+ cells; none changed in NQO1*2 cells (Supplementary Figure 1).

The subtlety of proteins changing in abundance following drug treatment suggested that other factors such as alterations in protein modifications and / or function were responsible for cell death. Phosphorylation of proteins is one of the most abundant and well characterized protein post-translational modifications and is a common signaling mechanism that may be altered by these drug treatments. Additionally, DNA damage is expected as a result of these drug treatments (11,12), and phosphorylation of proteins is a major contributor to the signaling and recruitment of DNA repair proteins. Therefore, we performed phosphoproteomics to determine if there are changes in the phosphorylation status of proteins involved in DNA repair and / or other cellular mechanisms. Phosphoproteomics using MS^3 identified a total of 5,863 proteins and 17,102 phosphopeptide groups (31,372 total peptide groups) across all NQO1+ treatment groups in the phosphoproteomics dataset (Figure 2) and 4,371 proteins and

12,206 phosphopeptide groups (18,486 total peptide groups) across all treatment groups in NQO1*2 cells (Supplementary Figure 2). Principle component analysis of NQO1+ samples shows that the DMSO and 15 µM Rucaparib replicates cluster together, while the sublethal 0.1 µM IB-DNQ, lethal dose 0.4 µM IB-DNQ, and combination treatment groups cluster away from these groups (Figure 2a). Rucaparib clustering with DMSO is reasonable because, without induction of DNA damage, there will not be much of an effect from the drug targeting DNA repair. This also confirms that this concentration of Rucaparib is non-lethal, which agrees with cell survival seen previously with single agent Rucaparib treatment (11). Similarly, there is only a small separation between the cluster for DMSO and the sublethal IB-DNQ dose alone. Interestingly, the 0.4 µM IB-DNQ and combination treatments cluster distantly from one another, suggesting that these two drug treatments have different downstream effects that lead to cell death.

In NQO1*2 samples, although we observe a similar number of changes with each treatment group, the greatest number of significant changes resulted from combination treatment with 25 phosphopeptides increasing and 28 decreasing in abundance (Supplementary Figure 2). In NQO1+ cells, we observe more distinct changes as a result of the different drug treatments (Figure 2c-f). Again, we see that the combination treatment leads to the greatest number of significant phosphopeptide changes with 309 increasing and 355 decreasing (Figure 2f). Gene ontology analysis of the proteins with significantly changing phosphorylation shows significant enrichment of pathways

involved in DNA repair, RNA processing, and other processes consistent with DNA damage response and transcription (Figure 2b).

The greater number of phosphorylation changes observed with NQO1+ compared to NQO1*2 shows that NQO1 is required for broader impacts on phosphorylation. This result is unsurprising because NQO1 is needed to activate IB-DNQ and is favorable because NQO1 is upregulated in cancer cells compared to normal tissue making IB-DNQ a strong candidate for cancer cell targeting by bioactivation. We also observe a synergistic effect of combining the sublethal 0.1 µM IB-DNQ and 15 µM Rucaparib treatments which supports the potential use of these drugs in a combination therapy.

Kinase substrate enrichment analysis predicts changes in DNA damage response and cell cycle regulation

To ascertain the kinases associated with the changing phosphorylation sites, we used a computational approach called Kinase Set Enrichment Analysis (KSEA) (26).This analysis predicts kinase activity from phosphoproteomics datasets by utilizing prior knowledge of kinase-substrate relationships from curated databases or computational prediction tools (26–29). Each kinase is scored based on the relative hyperphosphorylation and hypophosphorylation of its substrates, as identified from PhosphoSitePlus and NetworkIn (28,30,31). The positive and negative values represent an increase or decrease in inferred kinase activity in response to drug treatment relative to control, and blue and red bars in the bar plots represent kinases with significantly changing activity (Figure 3 and Supplementary Figure 3). With 0.1 µM IB-DNQ

treatment, PRKCB is the only kinase predicted to have significantly decreased activity, and 12 kinases are predicted to have increased activity (Supplementary Figure 3a). Two kinases, PRKCB and CDK7, are predicted to have decreased activity following Rucaparib treatment (Supplementary Figure 3b). Following 0.4 µM IB-DNQ treatment, 4 kinases are predicted to have increasing activity and 2 kinases are predicted to decrease in activity (Supplementary Figure 3c). With combination treatment, 3 kinases have decreased activity and 14 kinases have increased activity (Figure 3a). CDK1 and CDK2, which are essential for promoting cell cycle progression reviewed in (32) are predicted to have significantly decreased activity. Decreased activity of CDK1 and CDK2 is consistent with stalling of the cell cycle. NEK2, AURKC, RPS6KA2, PAK2, and PLK1 are also involved in cell cycle regulation reviewed in (33–37) and are predicted to have increased kinase activity. ATM and CHEK1, which positively regulate DNA damage response (32,38), also have significantly increased activity, which aligns with increased DNA damage we expect from the drug treatment. It is interesting that cell cycle regulation and DNA damage response are the most prevalent cellular mechanisms affected as these two mechanisms are highly targeted in cancer therapies, further strengthening the argument for the potential use of this combination treatment for TNBC patients. Based on these results, we decided to further investigate the changes involved in cell cycle regulation and DNA damage response.

Protein thermal stability impacted by single and dual agent treatments

Proteome-wide changes to protein-protein interactions, post-translational modifications, folding, and other biophysical properties of proteins can be assessed using thermal

proteome profiling (TPP) (39–43). TPP is used to determine thermal stability of each protein under different conditions, which are then analyzed computationally to identify proteins and mechanisms impacted by treatment (44,45). Analysis of TPP data with the R-package InflectSSP produces melt curves and calculates melt temperatures (T_m) and significant shifts in protein melt temperature. (45). TPP has been widely used to determine drug-target engagement (43), therefore we can apply it to test and compare the proteome-wide impacts on protein thermal stability across the different drug treatments. Compared to DMSO control, 713 proteins changed in stability when treated with 0.1 µM IB-DNQ, 1541 proteins changed in stability when treated with 0.4 µM IB-DNQ, 1824 proteins changed in stability with 15 µM Rucaparib, and 135 proteins changed in stability with combination treatment (Supplementary Figure 4a). With Rucaparib treatment, PARP1 appears to have a decreased thermal stability compared to DMSO treatment, but this was not determined to be statistically significant ($p=0.0646$; Supplementary Figure 4b). NQO1 thermal stability is unchanged when cells are treated with 0.1 or 0.4 µM IB-DNQ (Supplementary Figure 4c-d). This is likely due to the fact that IB-DNQ is a substrate for NQO1, and the transient IB-DNQ-NQO1 interaction is not sufficient to alter thermal stability. Although interesting, it is not surprising that we do not see these drugs affecting the stability of the target proteins.

Combination drug treatment increases H2AX phosphorylation and decreases stability

Histone protein H2AX phosphorylation at serine 139 (γH2AX) is a canonical marker for DNA damage reviewed in (46,47). The S139 residue of H2AX is phosphorylated by the

kinases ATM and ATR (48,49). Tyrosine 142 (Y142) of H2AX is constitutively phosphorylated and is gradually dephosphorylated in response to DNA damage (50). However, phosphorylation of S132 and Y142 at the same time prevents recruitment of repair proteins to S139 and may promote an apoptotic response (51). We observe significantly increased phosphorylation of H2AX at S139 and Y142 in NQO1+ cells treated with the combination drug but not with any of the single agent treatments (Figure 2c-f). Consistent with these results, KSEA predicted increased kinase activity of ATM (Figure 3). This suggests that IB-DNQ-induced DNA damage is being repaired in the absence of Rucaparib treatment, and the combination drug treatment leads to an accumulation of DNA damage. To determine if H2AX thermal stability was affected by the drug treatments, we analyzed the melt temperature and melt curves of H2AX under each condition. Due to the conditions of the InflectSSP workflow, the melt curve for H2AX in DMSO treated cells varies slightly with the comparison being made (44). The average melt temperature for H2AX in DMSO is 64.9ºC (Figure 4). Surprisingly, despite no change in phosphorylation, we observed significant destabilization of H2AX in 0.4 µM IB-DNQ with a decrease in melt temperature of 8.53ºC (Figure 4b, p=0.0465). We also observed significant destabilization of H2AX with the combination treatment where the melt temperature decreased 8.75ºC (Figure 4d, p=0.0193). However, the shape of the melt curve changes in the combination treatment with respect to DMSO (Figure 4d), suggesting different melt properties for H2AX with combination treatment compared to other drug treatments. This result suggests that the increased phosphorylation of H2AX following the combination treatment could alter the melt profile and melt temperature of the protein. This could be due to the phosphorylation event itself changing the

biophysical properties of H2AX or due to changes in other interactions that occur during the downstream DNA repair processes associated with γH2AX.

DNA repair and associated proteins have increased thermal stability following combination treatment

TPP data can also be evaluated using thermal proximity coaggregation analysis (TPCA). While melt shift analysis helps identify proteins with biophysical changes, TPCA is a method that specifically monitors binary protein interactions and protein complex dynamics (39). For this analysis, we used the Rtpca R-package which uses annotated protein interaction databases and measures Euclidean distance between protein melt curves to determine protein-protein interaction changes (52). Decreasing distance between melt curves suggests greater interaction between the two proteins, while increasing distance between curves indicates a reduced interaction. TPCA of combination drug treatment compared to DMSO TPP data reveals changes in protein-protein interactions and protein complex assembly. Figures 5a and 5b are volcano plots displaying TPCA coaggregation score of all binary protein interactions against $-\log_{10}$(p-value). Coaggregation score is determined by comparing the average melt curve distance in drug and DMSO (i.e. distance in drug – distance in DMSO). Therefore, positive coaggregation scores indicate decreased protein binary interaction while negative coaggregation scores indicate an increase in binary interactions. Proteins involved in DNA repair processes are highlighted in blue (Figure 5a). Upon analyzing the TPCA results, we identified that multiple subunits of the SWI / SNF complex, a protein complex involved in chromatin remodeling during DNA replication, transcription,

and DNA repair (53), were significantly changing in interaction with respect to each other (Figure 5b, highlighted in orange). We were specifically interested in the subset of SWI / SNF proteins that were increasing in interactions with one another as this could indicate tighter association of protein complexes and proteins that work together resulting in enhanced function. In DMSO, curves for these proteins are loosely associated, but in combination drug treatment, curves become more tightly associated indicating a stronger interaction in the combination drug treatment (Figure 5c). Protein-protein interaction network analysis using STRING shows known interactions between all 6 of these proteins (Figure 5d). The top 3 functional enrichments were chosen to categorize the biological processes in which these proteins are involved.-These finding suggests that chromatin remodeling by the SWI / SNF complex may be increased following the combination drug treatment.

Protein-protein interaction changes between cell cycle regulators

Our observations of differential kinase activity for several cell cycle regulatory proteins lead us to hypothesize that interactions between cell cycle regulators were changing with combination treatment, so we used TPCA to focus specifically on these proteins. Figure 6a highlights binary protein interaction changes between proteins involved in cell cycle regulation (yellow). p53 and TUBA1A, which interact at the mitotic centrosome (54,55), are shown to have a decreased interaction with the combination drug treatment (Figure 6a and c). In DMSO, the curves are tightly associated indicating a strong interaction, but the combination drug treatment weakens the interaction between p53 and TUBA1A as shown by the separation of the curves (Figure 6c; $p = 0.0066$). Several

binary protein interactions between CDK1 targets are both increasing and decreasing in interaction suggesting a change in function of CDK1 following combination treatment (Figure 6b, green points). Nine binary interactions between CDC20 and known interactors have stronger interactions in the combination drug treatment compared to DMSO indicating a potentially important role for CDC20 in response to combination treatment. Protein-protein interaction network analysis using STRING provides visual representation of the protein interactions that occur between the group of proteins that are increasing in interaction with CDC20 (Figure 6d). These proteins are involved in chromosome organization, regulation of mitosis, and microtubule organization. Our results suggest that the cell cycle is altered, potentially in an attempt to resolve problems caused by the dual agent treatment.

Dual and single treatments have distinct mechanisms leading to cell death

Single agent treatment with NQO1-bioactivatable drugs and combination treatment of NQO1 bioactivatable drugs and Rucaparib are both cancer cell death-inducing treatments (6,7,9,11). We performed a direct multi-omics comparison between the two treatments to analyze the mechanisms leading to cell death. Figure 7a compares changes in protein thermal stability between the two treatment groups. There are 22 total overlapping proteins. Interestingly, 16 proteins are destabilized in the lethal IB-DNQ treatment that are stabilized in the combination treatment. The few number of overlapping proteins, most of which are changing in opposite directions, suggests that the addition of the Rucaparib alters the mechanism by which cell-death is induced in these cells. Figure 7b compares changes in phosphorylation of peptides between the

two treatment groups. There are 34 peptides that have decreased phosphorylation and 16 peptides with increased phosphorylation in both treatment groups. 18 phosphopeptides are significantly changing in both treatments but in opposite directions. Several of the proteins with phosphopeptides that are increasing with combination treatment and decreasing with 0.4 µM IB-DNQ are involved in RNA splicing regulation, as identified by PANTHER Gene Ontology analysis (data not shown). These include DDX23, SRSF7, SRRM2, SRRM1, CDK12, and others. This suggests differential alterations to mRNA splicing and potentially protein translation depending on the treatment.. The low number of overlapping changes between the two lethal treatment groups suggests that these have different targets. The distinct changes caused by these two different drug treatments may explain the increased efficacy of the dual agent treatment.

Finally, we analyzed overlaps in proteins with thermal stability and phosphorylation changes between the different IB-DNQ treatment groups - low dose, high dose, combination (Supplementary Figure 5). The greatest number of overlaps occurs between low dose and high dose IB-DNQ protein stability changes, which is unsurprising and validates the reproducibility of the IB-DNQ effects seen in these cells.

DISCUSSION

TNBC accounts for a large portion of breast cancer diagnoses, and treatment for these patients is limited. Even with the most modern therapies, the risk of metastases and tumor recurrence is high (1,2). Research is ongoing to develop tumor-type specific

treatment options that are highly effective with limited toxicity. Previous studies have shown that NQO1 bioactivatable drugs, including β-lapachone and IB-DNQ, induce cell death of tumors with elevated expression of NQO1 (6,7). Further, dual agent treatment of NQO1+ tumors with β-lapachone and the PARP1 inhibitor Rucaparib has shown to increase efficiency of treatment (11), but the cellular processes affected by this combination treatment were not well understood. Here we show that combining a low dose of IB-DNQ and Rucaparib induced changes in cell cycle regulators and DNA damage repair proteins in an NQO1-dependent manner.

We observe a greater number of changes to protein abundance and phosphorylation when NQO1 is increased compared to when NQO1 is low (Figures 1 and 2). These results further support the specificity of IB-DNQ for cells with increased NQO1 levels and strengthen the potential use of these drugs in TNBC patients. We also observe a synergistic effect from the combination drug treatment complementary to what was seen with b-lapachone and Rucaparib (11). We observed a greater number of changes in protein abundance and phosphorylation with dual agent treatment than what would be expected if the treatments provided an additive effect (Supplementary Figure 1 and Figure 2). The predominant mechanisms found to be affected by the IB-DNQ and Rucaparib dual agent treatment are DNA damage response and cell cycle regulation (Figures 5 and 6), which are both highly targeted mechanisms in cancer treatments (56). We did not expect to see large changes in apoptotic signaling mechanisms as this was a short treatment time that was ended before cell death could take place. The changes we did observe point to the mechanisms that protect the cells before

apoptosis. Further studies analyzing longer treatment times are needed to determine onset of apoptotic response.

Increased phosphorylation of H2AX at S139, which is indicative of increased DNA damage (46), has been observed previously upon treatment of NQO1+ cells and NQO1+ xenograft models with combination treatment of β-lapachone and Rucaparib (11). Our experiments replicate that finding and additionally show that dual agent treatment increases phosphorylation of Y142 of H2AX, which, in combination with increased S139 phosphorylation, suggests the cells are moving towards apoptosis (51). We likely only observe this with the dual agent treatment because DNA damage is accumulating as the cell is not able to repair the DNA with PARP1 inhibition. We also show that H2AX protein is destabilized under these conditions, and considering the phosphorylation status of H2AX, we can hypothesize that the increased phosphorylation contributes to the decreased stability of H2AX. Presence of phosphorylated S139 and Y142 prevents recruitment of DNA damage repair proteins at these sites (51), which may also contribute to the stability change of H2AX following DNA damage. Additionally, the decreased stability of H2AX suggests alterations to chromatin organization, potentially for DNA repair or in preparation for apoptosis in response to the dual agent treatment. Our results indicate increased DNA damage and reduced DNA repair are a result of the dual agent treatment, and together these suggest the cancer cells are unable to escape cell death, further supporting the potential use of this dual agent as TNBC therapeutic.

Analysis of protein-protein interactions using thermal profiling and TPCA revealed changes in interactions between proteins involved in the SWI / SNF complex following dual agent treatment. SWI / SNF is known to be involved in DNA repair processes, as its role in chromatin remodeling makes damaged DNA accessible to repair proteins (57–60). Our results suggest that the increased DNA damage caused by the dual agent treatment leads to an increased requirement of chromatin remodeling, and therefore increased interactions within the SWI / SNF complex. TPCA also indicated a decreased interaction between cd and tubulin with the combination treatment. Others have shown that p53 is directly associated with microtubules and is involved in centrosome duplication (54,55) and that inhibition of p53 localization to the mitotic centrosome results in breakdown of the centrosome and cell death (61). Taking this into consideration, the observed decreased interaction between p53 and tubulin could be due to altered microtubule dynamics resulting in paused cell cycle. We propose that the accumulation of DNA damage from the dual agent treatment stalls the cell cycle in an attempt to repair DNA prior to division and ultimately leads to cell death.

CONCLUSIONS

Together, our results show that combination treatment of IB-DNQ and Rucaparib is a promising tumor-specific treatment that targets cell cycle and DNA damage repair only in cells with highly expressed NQO1. Future studies in mammalian systems and TNBC patients are needed to better understand the efficacy and toxicity of this dual agent treatment when tissue and organ systems come into play.

METHODS

Cell culture and drug treatment

MDA-MB-231 triple negative breast cancer cells were obtained from the American Tissue Culture Collection (ATCC, Manasas, VA). These cells natively express the NQO1*2 polymorphism; NQO1 positive cells were generated by overexpressing NQO1 by plasmid transfection. Cells were cultured under 5% CO2-95% air atmosphere at 37 °C, in DMEM (Life Technologies, Carlsbad, CA) containing 5-10% fetal bovine serum (Hyclone, Thermo Sci., Logan UT). All cells were mycoplasma-free. NQO1 positive and NQO1*2 cells were treated with 0.1 μM IB-DNQ (2 hours), 0.4 μM IB-DNQ (2 hours). 15 μM Rucaparib (4 hours), or 0.1% DMSO (2 hours). For the combination treatment, cells were pretreated with 15 μM Rucaparib for 2 hours, then co-treated with 0.1 μM IB-DNQ and 15 μM Rucaparib for 2 hours. All drugs and DMSO were prepared in 5% DMEM.

Sample preparation for global and phosphoproteomics

Approximately 10 million cells were collected per treatment condition (n=3). Proteins were extracted by denaturing with 8M urea, followed by LysC / Trypsin Gold (Promega) digestion. Forty-five μg of protein was used for global analysis and 3 mg was used for phosphopeptide enrichment. Phosphopeptides were enriched by applying the 3 mg samples prepared above to High-Select TiO_2 Phosphopeptide Enrichment tips (A32993, Thermo Fisher Scientific). Tips were washed and eluted using vendor-described protocols.

TPP sample preparation

Approximately 10 million cells were collected per treatment condition (n=2). Cells were resuspended in NP-40 lysis buffer (40 mM HEPES (pH 7.5), 200 mM NaCl, 5 mM b-glycerophosphate, 0.1 mM sodium orthovanadate, Roche EDTA free complete protease inhibitor, 2 mM TCEP, 0.4% NP-40) and sonicated in a Bioruptor sonication system from Diagenode Inc. (30-s / 30-s on / off cycles for 30 min, 4°C). Following centrifugation at 12,000*g* for 15 min, protein concentrations were determined using a Bradford protein assay (5000002, Bio-Rad). Samples were adjusted to the same concentration and divided equally into 8 tubes for heat treatment in the thermocycler (25ºC for 3 minutes, 3 minutes at temperature gradient, 25ºC for 3 minutes). Temperature gradient is as follows: 25ºC, 35ºC, 39.3ºC, 50.1ºC, 54.8ºC, 60.7ºC, 74.9ºC, 90ºC. Each sample was centrifuged to pellet aggregated protein, and supernatant was reserved. Proteins were precipitated in 20% trichloroacetic acid (TCA) overnight and washed with acetone. Precipitated proteins were resuspended in 8M Urea in 100 mM HCl (pH 8.0). Proteins were reduced with 5 mM tris(2-carboxyethyl)phosphine (TCEP) and alkylated with 10 mM chloroacetaminde. Samples incubated with Trypsin / Lys-C mix (1:70 protease:substrate ratio; V5072, Promega) for 4 hours, then were diluted with 100 mM Tris-HCl to reduce urea concentration to less than 1M and digested overnight. Digestion was quenched with 0.4% trifluoroacetic acid (TFA).

Peptide purification, TMT-labeling, and high-pH basic fractionation

Peptides were desalted on a 50 mg Sep-Pak C18 Vac (Waters Corporation) using a vacuum manifold. Peptides were eluted with 70% acetonitrile (ACN) and 0.1% formic

acid (FA), dried by speed vacuum, and resuspended in 50 mM triethylammonium bicarbonate (TEAB, pH 8.5). For global and phosphoproteomics samples, peptide concentration was measured using the Pierce Quantitative Colorimetric Peptide Assay Kit (23275, Thermo Fisher Scientific) to ensure an equal amount of each sample was labeled. Samples were then tandem mass tag (TMT)-labeled for 2 hours at room temperature. Labeling reaction was quenched with 5% hydroxylamine, and labeled peptides were mixed together. Peptide mixtures were desalted and fractionated using 50 mg Sep-Pak C18 Vac columns (Waters Corporation). Peptides were eluted in 12.5%, 15%, 17.5%, 20%, 22.5%, 25%, 30%, and 70% acetonitrile in 0.1% triethylamine. Fractions were dried in speed vacuum and resuspended in 0.1% formic acid.

Global proteomics data acquisition: Nano-LC-MS / MS

Nano-LC–MS / MS analyses were performed on an Orbitrap Fusion Lumos mass spectrometer (Thermo Fisher Scientific) coupled to an EASY-nLC HPLC system (Thermo Fisher Scientific). Each fraction was loaded onto a reversed-phase PepMap RSLC C18 column with an Easy-Spray tip at 400 nl / min (ES802A, Thermo Fisher Scientific; 2 µm, 100 Å, 75 µm by 25 cm). Peptides were eluted from 4 to 35% B over 160 min, 35 to 50% B for 14 min, and dropping from 50 to 10% B over the final 1 min (mobile phases A: 0.1% FA and water; B: 0.1% FA and 80% ACN). Mass spectrometer settings include a capillary temperature of 300°C, and ion spray voltage was kept at 1.8 kV. The mass spectrometer method was operated in positive-ion mode with a 4-s cycle time data-dependent acquisition with advanced peak determination and Easy-IC on (internal calibrant). Precursor scans [mass / charge ratio (*m* / *z*), 400 to 1500] were

done with an Orbitrap resolution of 60,000, 30% RF (radio frequency) lens, 50-ms maximum inject time (IT) and automatic gain control (AGC) target of 400,000, including charges of 2 to 6 for fragmentation with 60-s dynamic exclusion. Higher-energy collisional dissociation (HCD) MS2 scans were performed at 50k Orbitrap resolution, fixed collision energy of 38%, AGC target of 10,000, and 86-ms maximum IT.

Phosphoproteomics data acquisition: Nano-LC-MS / MS / MS

Nano-LC–MS / MS / MS analyses were performed on an Orbitrap Fusion Lumos mass spectrometer (Thermo Fisher Scientific) coupled to an EASY-nLC HPLC system (Thermo Fisher Scientific). Each fraction was analyzed with the same LC conditions as above on a Lumos Orbitrap mass spectrometer (Thermo Fisher Scientific). Mass spectrometer settings include a capillary temperature of 300°C, and ion spray voltage was kept at 1.9 kV. The mass spectrometer method was operated in positive-ion mode with a 3-s cycle time data-dependent acquisition with advanced peak determination and Easy-IC on. Precursor scans (*m / z*, 400 to 1500) were done with an Orbitrap resolution of 120,000, 30% RF lens, 50-ms maximum IT, AGC target of 400,000, including charges of 2 to 7 for fragmentation with 90-s dynamic exclusion. Collision induced dissociation (CID) MS2 scans were performed at 30k Orbitrap resolution, fixed collision energy of 35%, AGC target of 50,000, and 60-ms maximum IT. HCD MS3 scans were performed at 50k Orbitrap resolution, fixed collision energy of 65%, AGC target of 100,000, and 105-ms maximum IT.

TPP data acquisition: Nano-LC-MS / MS

Nano-LC–MS / MS analyses were performed on an Orbitrap Exploris 480 mass spectrometer (Thermo Fisher Scientific) coupled to an EASY-nLC HPLC system (Thermo Fisher Scientific). Two technical replicates of each fraction were loaded onto a reversed-phase PepMap RSLC C18 column with an Easy-Spray tip at 400 nl / min (ES802A, Thermo Fisher Scientific; 2 µm, 100 Å, 75 µm by 25 cm). Peptides were eluted from 6 to 32% B over 180 min, 10 to 32% B for 14 min, and dropping from 50 to 10% B over the final 1 min (mobile phases A: 0.1% FA and water; B: 0.1% FA and 80% ACN). Mass spectrometer settings include a capillary temperature of 300°C, and ion spray voltage was kept at 1.9 kV. The mass spectrometer method was operated in positive-ion mode with a 1.3-s cycle time data-dependent acquisition with advanced peak determination and Easy-IC on (internal calibrant). FAIMS CVs cycled through -45, -55, and -70 V. Precursor scans [mass / charge ratio (*m* / *z*), 375 to 1500] were done with an Orbitrap resolution of 60,000, 40% RF lens, normalized AGC target of 200%, including charges of 2 to 8 for fragmentation with 60-s dynamic exclusion. Higher-energy collisional dissociation (HCD) MS2 scans were performed at 45k Orbitrap resolution, normalized collision energy of 32%, normalized AGC target of 200%.

Protein identification and quantification – global proteomics

Resulting MS2 RAW files were analyzed in Proteome Discoverer 2.5 (Thermo Fisher Scientific) with FASTA databases including UniProt human sequences plus common contaminants such as proteolytic digestion enzymes. Quantification methods used isotopic impurity levels available from Thermo Fisher Scientific. SEQUEST HT searches were conducted with a maximum number of two missed cleavages, a precursor mass

tolerance of 10 parts per million, and a fragment mass tolerance of 0.02 Da. Static modifications used for the search were (i) carbamidomethylation on cysteine (C) residues and (ii) TMT6plex labels on lysine (K) residues and the N termini of peptides. Dynamic modifications used for the search were oxidation of methionine, acetylation of N termini, and N-terminal loss of methionine with and without acetylation. Percolator false discovery rate (FDR) was set to a strict setting of 0.01 and a relaxed setting of 0.05. Values from both unique and razor peptides were used for quantification. In the consensus workflow, peptides were normalized by total peptide amount with scaling to mixed sample control. Global proteomics data have been deposited with ProteomeXchange repository, project accession: XXXX.

Protein identification and quantification – phosphoproteomics

Resulting MS3 RAW files were analyzed in Proteome Discoverer 2.5 (Thermo Fisher Scientific) with FASTA databases including UniProt human sequences plus common contaminants. Quantification methods used isotopic impurity levels available from Thermo Fisher Scientific. SEQUEST HT searches were conducted with a maximum number of two missed cleavages, a precursor mass tolerance of 10 parts per million, and a fragment mass tolerance of 0.02 Da. Static modifications used for the search were (i) carbamidomethylation on cysteine (C) residues and (ii) TMT6plex labels on lysine (K) residues and the N termini of peptides. Dynamic modifications used for the search were phosphorylation of serine, threonine, and tyrosine, oxidation of methionine and tryptophan, acetylation of N termini, and N-terminal loss of methionine with and without acetylation. Percolator false discovery rate (FDR) was set to a strict setting of

0.01 and a relaxed setting of 0.05. Values from both unique and razor peptides were used for quantification. In the consensus workflow, SPS Mass Matches threshold was 0, and peptides were normalized by total peptide amount with scaling to a mixed sample control. Phosphoproteomics data have been deposited with ProteomeXchange repository, project accession: XXXX.

Protein identification and quantification – TPP

Resulting MS2 RAW files were analyzed in Proteome Discovererä 2.5 (Thermo Fisher Scientific) with FASTA databases including UniProt human sequences plus common contaminants. Quantification methods used isotopic impurity levels available from Thermo Fisher Scientific. SEQUEST HT searches were conducted with a maximum number of three missed cleavages, a precursor mass tolerance of 10 parts per million, and a fragment mass tolerance of 0.02 Da. Static modifications used for the search were (i) carbamidomethylation on cysteine (C) residues and (ii) TMTpro labels on lysine (K) residues and the N termini of peptides. Dynamic modifications used for the search were oxidation of methionine, acetylation of N termini, and N-terminal loss of methionine with and without acetylation. Percolator false discovery rate (FDR) was set to a strict setting of 0.01 and a relaxed setting of 0.05. Values from both unique and razor peptides were used for quantification. In the consensus workflow, peptides were normalized by total peptide amount with no scaling. No normalization was performed for TPP experiments. Thermal proteome profiling data have been deposited with ProteomeXchange Consortium, project accession: XXXX.

Analysis of TPP data

The InflectSSP R-package (v 1.6) in R Studio (R Studio for Mac, version 2022.12.0+353) was used for curve fitting, melt temperature, and melt shift analysis. Accession numbers, number of PSMs, number of unique peptides, and abundance values for each condition were divided into separate Excel files. InflectSSP parameters were set as follows: NControl = 2, NCondition = 2, PSM = 0, UP =0, CurveRsq = 0, PValMelt = 0.05, MeltLimit = 0, STRINGScore = 0.99. Differential thermal proximity coaggregation analysis was conducted using the R package *Rtpca* (52) with the normalized and corrected abundances from the InflectSSP output. Only melt curves with an R-squared value >= 0.7 were used. For a given protein, the abundance values of biological replicates were averaged for each temperature for each condition. First, complexes with co-aggregation were tested using the runTPCA function and the CORUM human protein complex annotations with number of sampling set for 100,000 for each condition. Protein complexes with a p-value less than 0.15 in at least one condition were further analyzed for differential thermal proximity coaggregation between the two conditions. Differential TPCA was conducted using the runDiffTPCA function where the protein-protein interaction annotation was derived from BioGRID. Protein pairs with a p-value <= 0.05 were considered to have differential thermal proximity coaggregation. The list of CDK1 targets was obtained from Uniprot as of May 5, 2023. Volcano plots were created using ggplot2. The melt curves of binary protein pairs with differential TPCA were graphed using the plotPPiProfiles functions from Rtpca. CORUM v.4 human protein complex annotations were downloaded from http://mips.helmholtz-

muenchen.de/corum/ (62,63). The physical protein-protein interaction data were used from BioGRID v.4.4.210 downloaded from https://thebiogrid.org (64).

Kinase Substrate Enrichment Analysis (KSEA) (26,27)

The KSEA web app was used for analysis of phosphoproteomics data. The algorithm takes an input file in *.csv* format consisting of a list of peptides, corresponding protein and gene names, phosphosites and associated fold change (FC) and p-values. The *p*-value cutoff and substrate count cutoff were set at 0.05 and 2, respectively. Kinase substrate relationships from both PhosphoSitePlus and NetworkIn to improve were used.

Gene Ontology and Protein Network Analysis

ShinyGo (version 0.80) was used to determine enrichment in phosphoproteomics data. Analyzed proteins contained phosphopeptides that were significantly changing ($p \geq 0.05$) in combination treatment (NQO1+) compared to DMSO. A background list containing all detected proteins was provided. FDR cutoff was set to 0.05. The PANTHER overrepresentation test (version 18.0) was used for gene ontology analysis of proteins with phosphopeptides increasing with combination treatment and decreasing with 0.4 µM IB-DNQ. A Fisher's exact test was used to calculate enrichment, and a false discovery rate was calculated. Protein-protein interaction networks were analyzed using STRING (version 12.0).

Data visualization

Volcano plots and PCA plots were created in R Studio using ggplot2(65) (version 3.4.2). Upset plots were created in R studio using UpSetR (66). Heatmap was created in ProteomeDiscoverer™ 2.5 (Thermo Fisher Scientific) using scaled abundance of peptide groups, Euclidean distance, Ward linkage method, and scaling before clustering.

Declarations

Ethics approval and consent to participate

Not applicable.

Consent for publication

Not applicable.

Competing interests

The authors declare that they have no competing interests.

Funding

Catherine Peachy Fund and P30CA082709 to A.L.M, T32CA2723370 to A.M.R., R01CA221158 to D.A.B. / E.A.M., F30AG079580 to H.R.S.W.

Author's contributions

A.M.R. – data acquisition, data analysis, writing and revision of manuscript

H.R.S.W. – data acquisition, data analysis, revision of manuscript

S.A.P.J. – writing and revision of manuscript

A.B.W. – data acquisition, data analysis

G.R. – data analysis

N.S. – experimental design, sample preparation

P.H. – development of IB-DNQ

D.A.B. – experimental design

E.A.M. – experimental design, revision of manuscript

A.L.M. – experimental design, data analysis, revision of manuscript

Acknowledgements

We thank Neil McCracken for support with data analysis using InflectSSP and Colton Starcher for assistance with cell culture. The mass spectrometry work performed in this work was done by the Indiana University School of Medicine Center for Proteome Analysis. Acquisition of the IUSM Center for Proteome Analysis' instrumentation used for this project was provided by the Indiana University Precision Health Initiative. The Center for Proteome Analysis receives support from 3UL1TR002529 and P30CA082709.

Footnotes

David Boothman is included as an author posthumously.

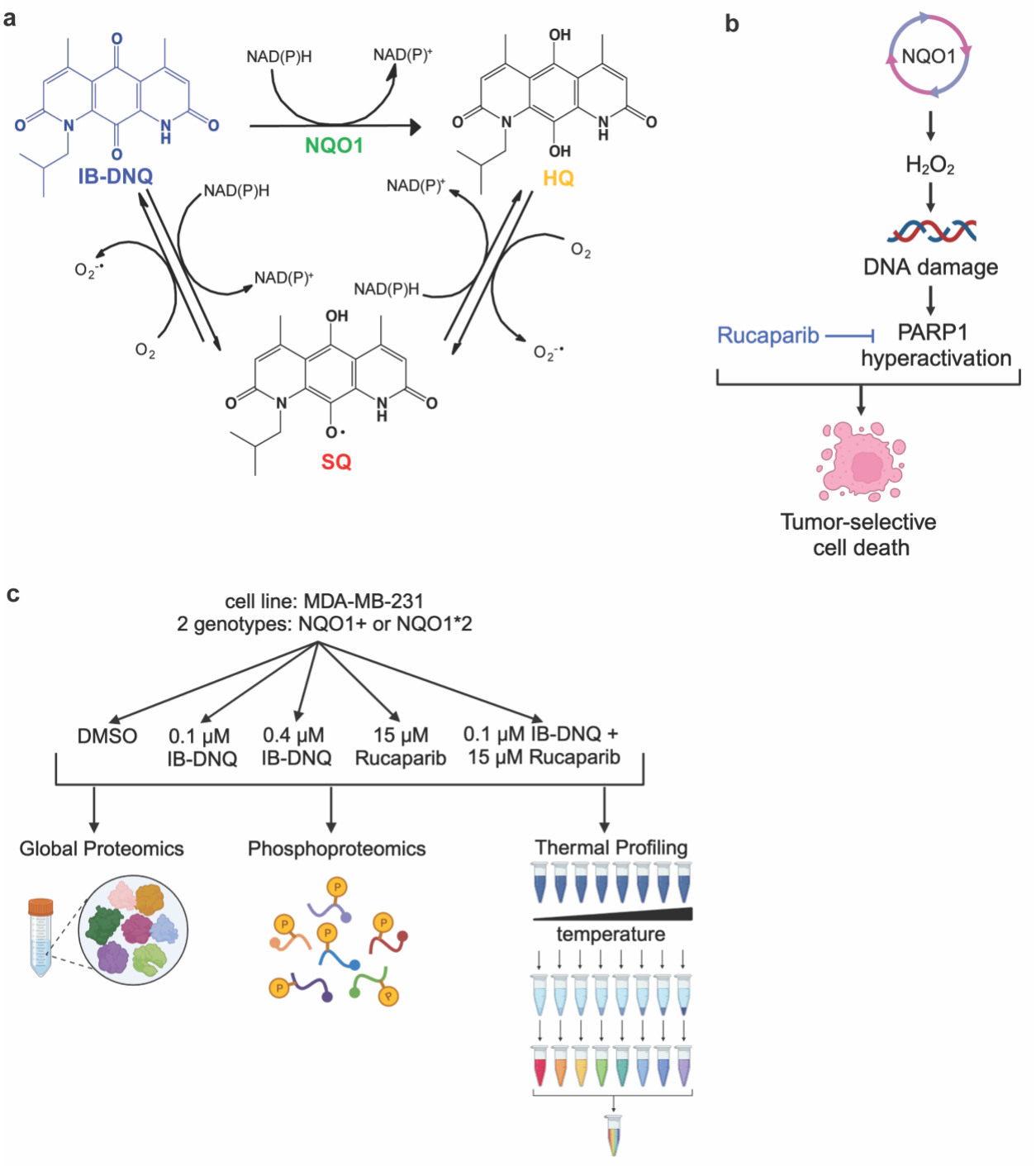

Figure 1: Treatment with the bioactivatable drug IB-DNQ in combination with PARP1 inhibitor, Rucaparib, leads to tumor-selective cell death. a) IB-DNQ acts as a futile cycling substrate for NQO1 which results in depletion of NAD(P)H and accumulation of reactive oxygen species. HQ = hydroquinone; SQ = semiquinone. Adapted from (67). b)

IB-DNQ treatment leads to DNA damage, and inhibition of PARP1-mediated DNA repair mechanisms via Rucaparib leads to tumor-selective cell death. c) MDA-MB-231 triple negative breast cancer cells altered with a vector to stably overexpress wild-type NQO1 or the variant NQO1*2 (containing empty vector control) were treated with DMSO, 0.1 µM (sublethal) or 0.4 µM (lethal) IB-DNQ, 15 µM Rucaparib, or a combination treatment of 0.1 µM IB-DNQ and 15 µM Rucaparib. Samples were analyzed using global proteomics, phosphoproteomics, and TPP.

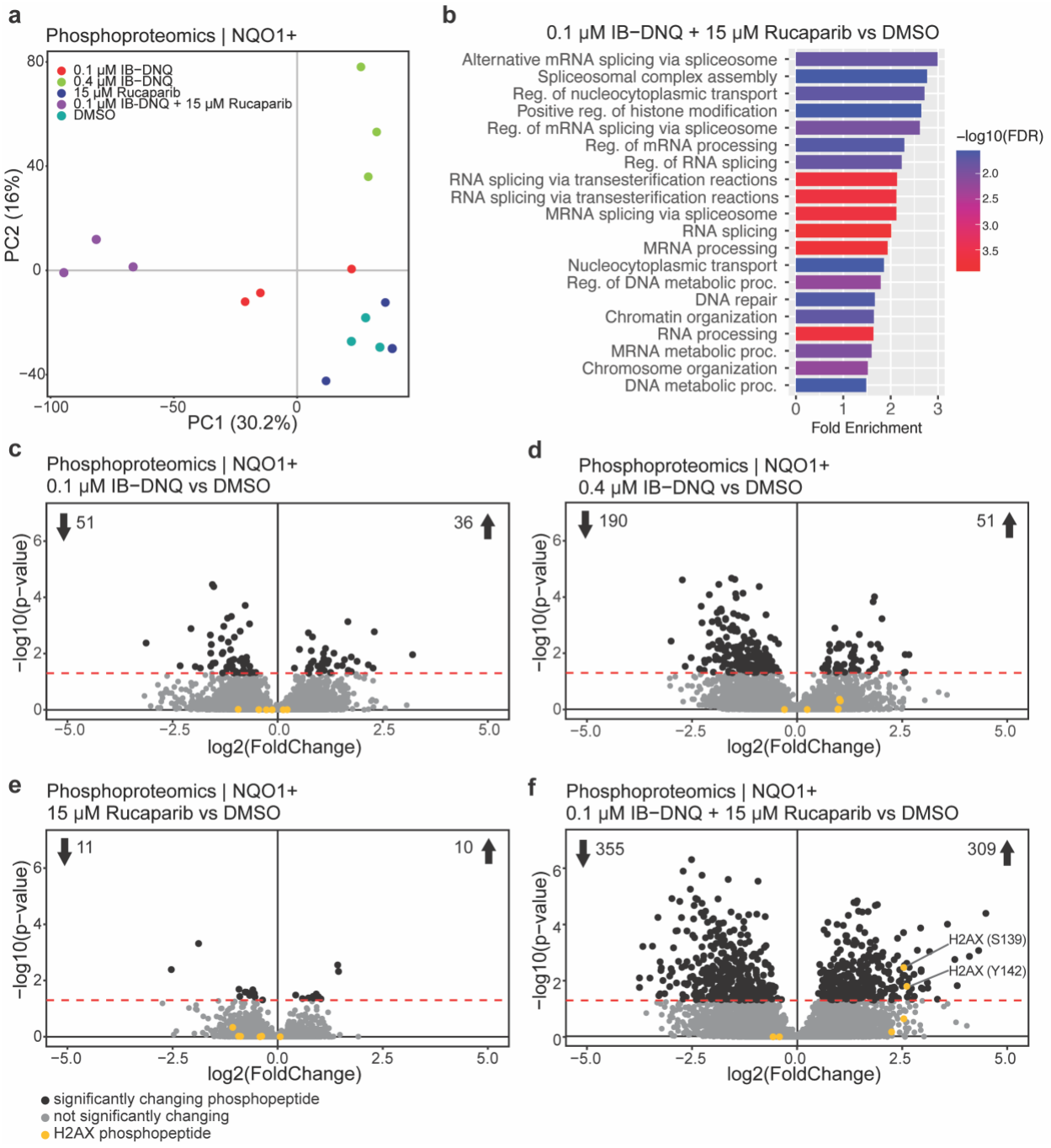

Figure 2: Large changes in phosphoproteome observed in combination treated NQO1+ cells. a) Principal component analysis of phosphoproteomics data from NQO1+ TNBC cells. Data was generated using scaled abundances of phosphopeptides groups that were quantified in all samples (n=3). Data from 3 independent replicates cluster

together. Combination treated cells cluster together, separately from other treatment groups. b) Gene ontology analysis of proteins with significantly changing phosphopeptides in combination treatment compared to DMSO. c-f) Volcano plots show differential phosphorylation of phosphopeptide groups in 0.1 µM IB-DNQ (c), 0.4 µM IB-DNQ (d), 15 µM Rucaparib (e), and combination (f) treated NQO1+ cells compared to DMSO treated cells. Yellow points represent phosphopeptides matching to the histone protein H2AX. H2AX S139 and Y142 peptide sequences: ATQAS(p)QEY and KATQASQEY(p). Red dashed line is p-value cut off p=0.05.

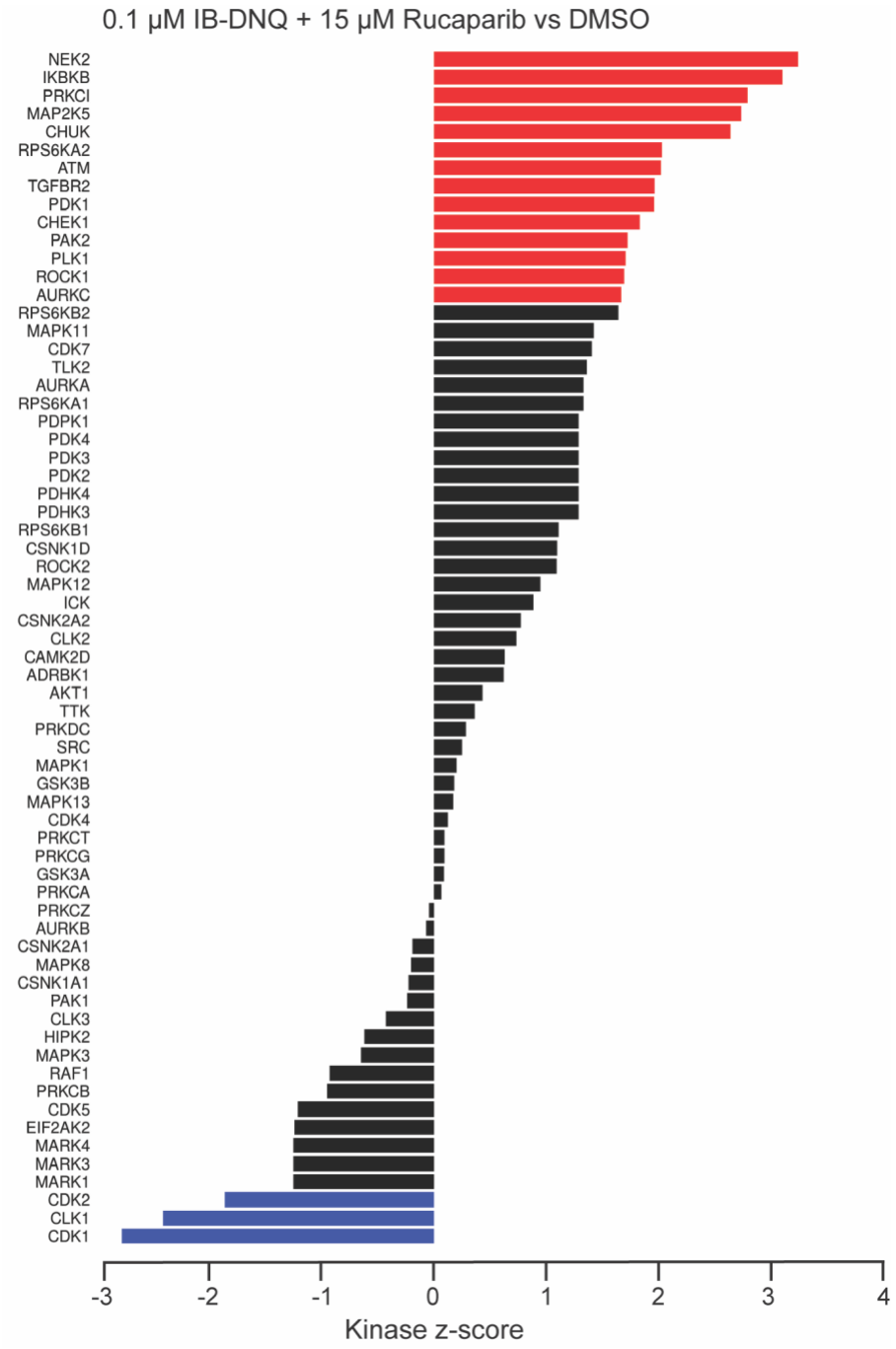

Figure 3: Kinase substrate enrichment analysis (KSEA) of combination drug treated cells compared to DMSO. KSEA bar plot for 0.1 μM IB-DNQ + 15 μM Rucaparib. Red bars indicate kinases with significantly increased inferred activity ($p<0.05$), and blue

bars indicate kinases with significantly decreased inferred activity. Black bars show kinases with differential inferred kinase activity but are not statistically significant.

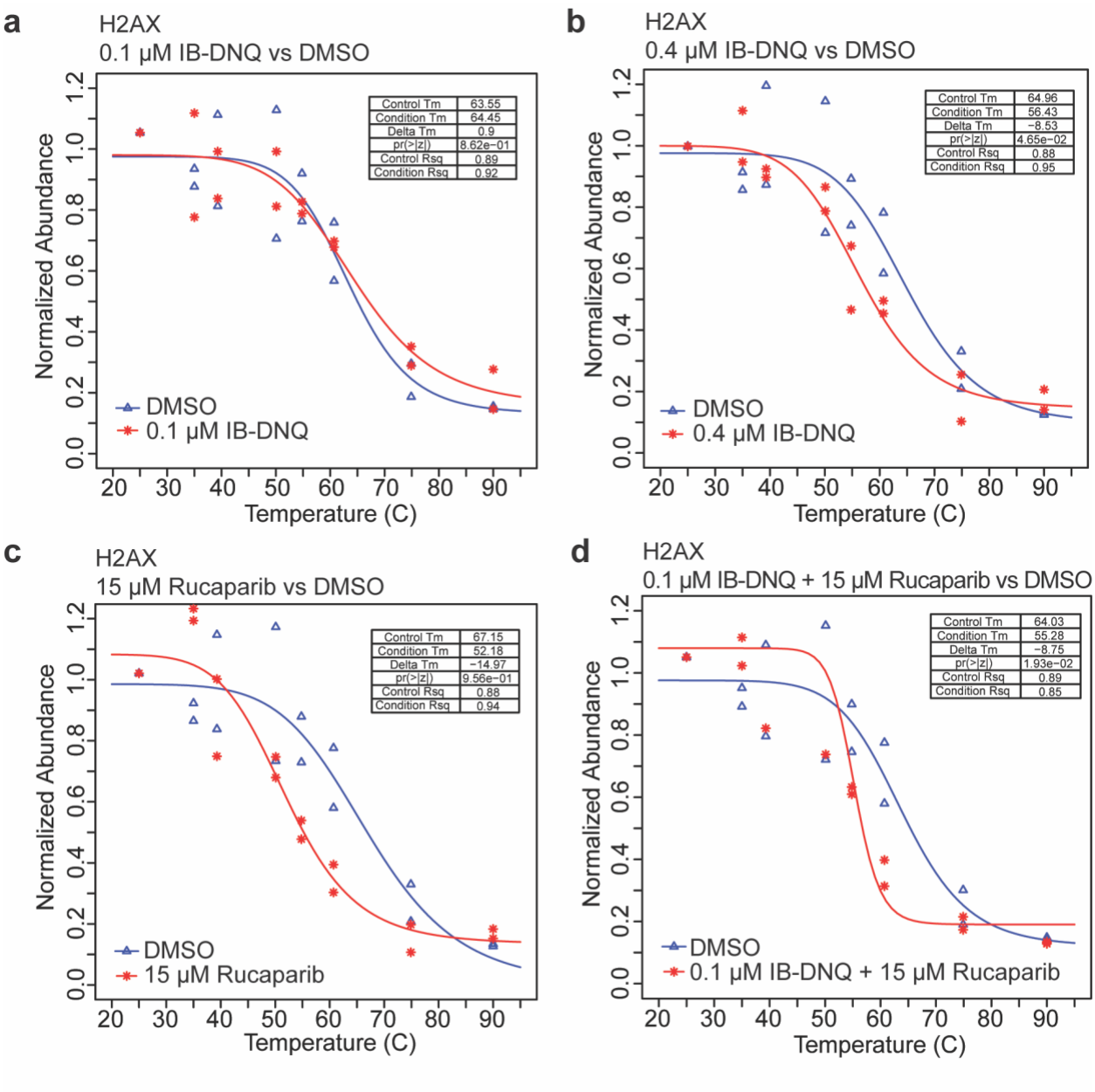

Figure 4: Thermal stability of H2AX following different drug treatments. a-d) Melt curves for H2AX in 0.1 μM IB-DNQ (a), 0.4 μM IB-DNQ (b), 15 μM Rucaparib (c), and combination drug (d) treated cells compared to DMSO as calculated by InflectSSP. Blue lines represent melt curves for H2AX in DMSO treated cells, and red lines represent melt curves for H2AX in drug treated cells. H2AX is significantly destabilized in 0.4 μM

IB-DNQ (ΔT_M = -8.53ºC, p = 0.0465) and combination (ΔT_M = -8.75ºC, p = 0.0193) treated cells.

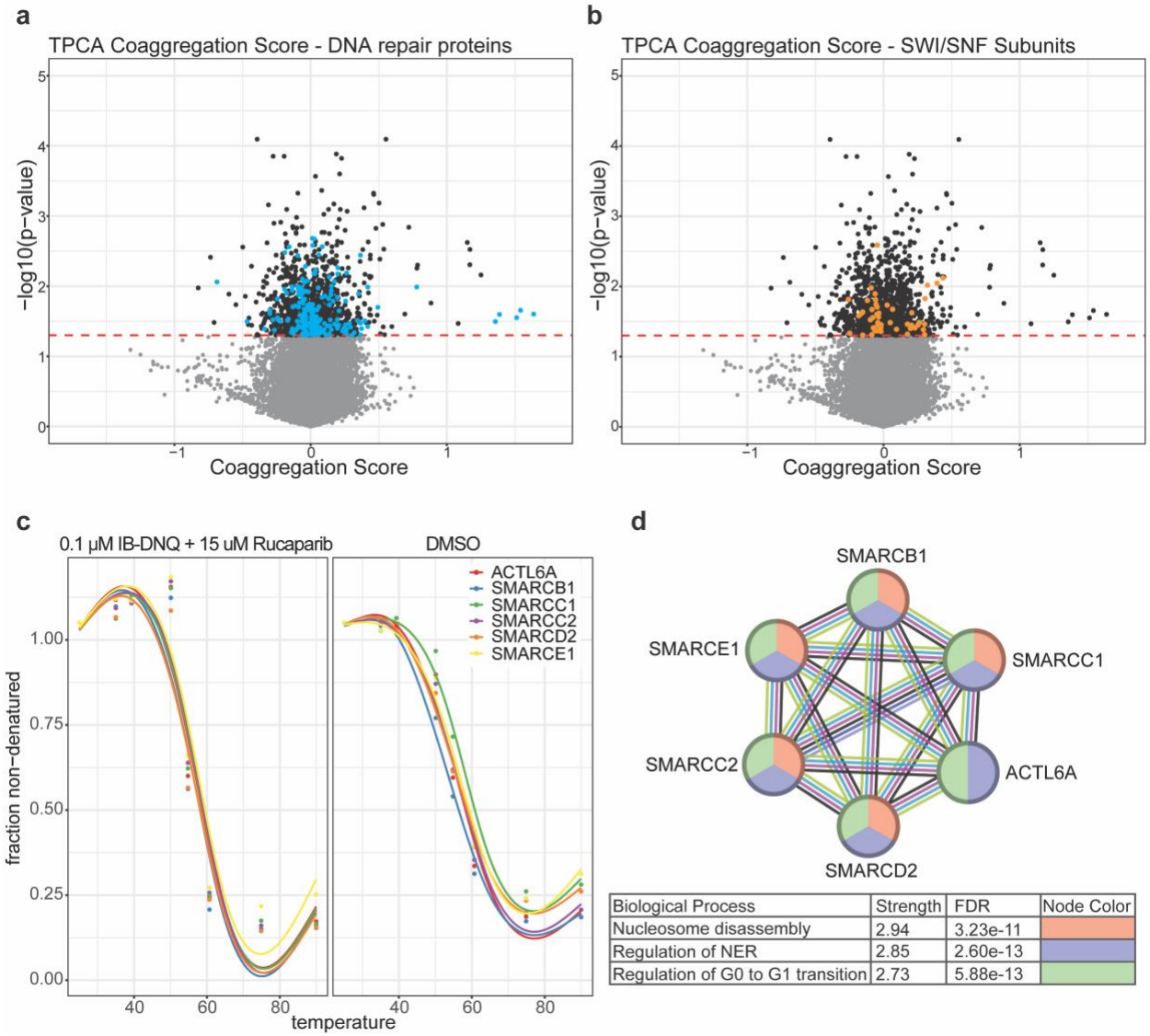

Biological Process	Strength	FDR	Node Color
Nucleosome disassembly	2.94	3.23e-11	
Regulation of NER	2.85	2.60e-13	
Regulation of G0 to G1 transition	2.73	5.88e-13	

Figure 5: Thermal stability of DNA damage repair proteins and chromatin remodeling complex SWI / SNF are affected by combination drug treatment. a,b) Volcano plots of differential protein coaggregation as identified by thermal proximity coaggregation (TPCA) in combination treatment compared to DMSO. Blue dots indicate protein pairs with significantly changed coaggregation involved in DNA damage repair (a) and orange dots indicate proteins in the SWI / SNF complex (b). Red dashed line is p-value cut off p=0.05. c) Melt curves for proteins involved in the SWI / SNF complex in DMSO and

combination treated cells. Tighter association of curves in combination treatment indicates tighter association of proteins in the complex compared to DMSO. d) Protein-protein interaction network of SWI / SNF proteins in c. The top 3 biological processes in terms of strength are shown. These proteins are involved in nucleosome disassembly, regulation of nucleotide excision repair (NER), and transition to G1 phase in the cell cycle. Node color corresponds to the complex the protein is involved in; color of lines connecting nodes corresponds to origin of protein-protein interaction annotation (black=co-expression, pink=experimentally determined, light blue=from curated database, green=textmining, purple=protein homology).

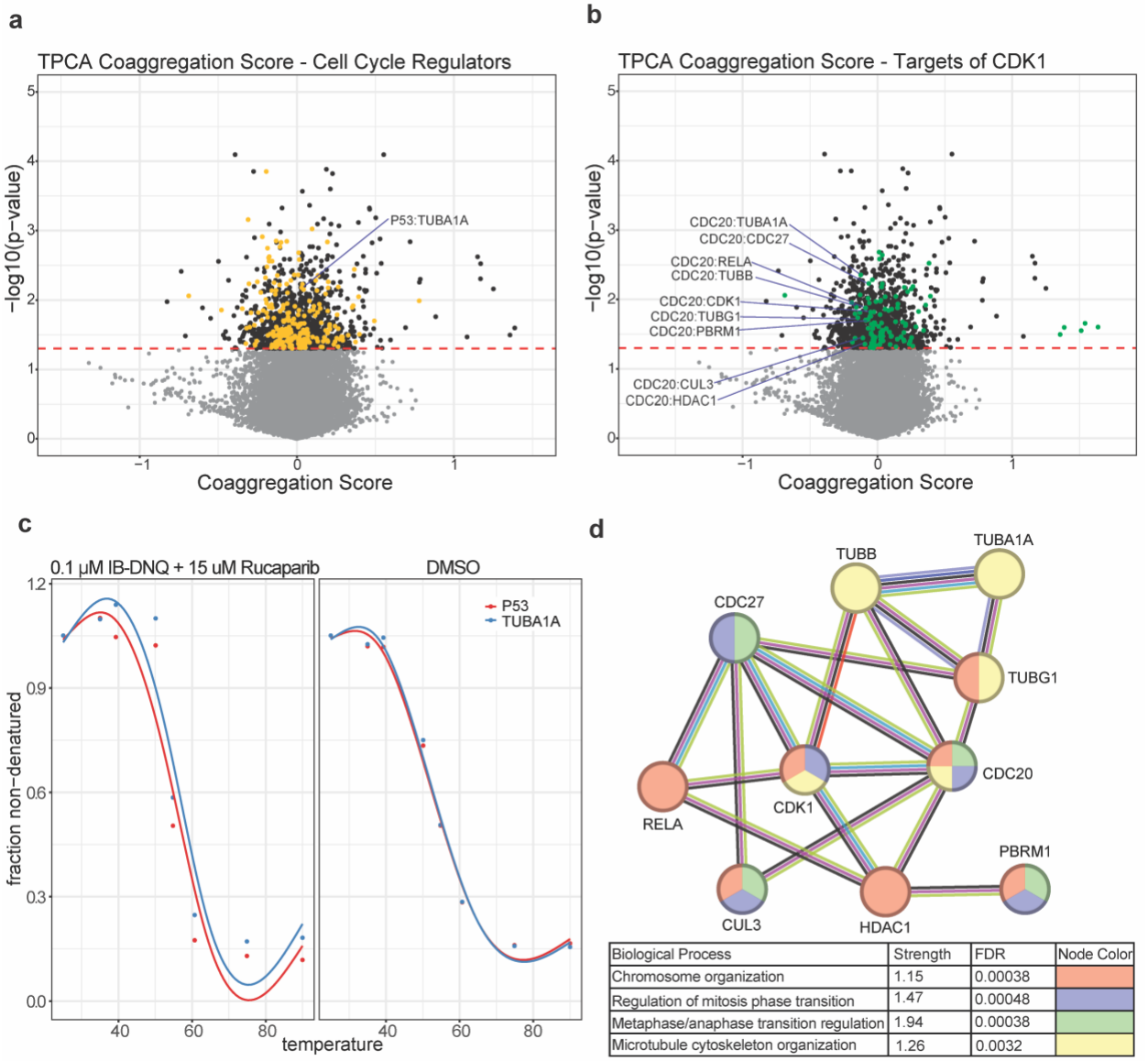

Biological Process	Strength	FDR	Node Color
Chromosome organization	1.15	0.00038	
Regulation of mitosis phase transition	1.47	0.00048	
Metaphase/anaphase transition regulation	1.94	0.00038	
Microtubule cytoskeleton organization	1.26	0.0032	

Figure 6: Thermal stability of cell cycle regulators and CDK1 targets are affected by combination drug treatment. a,b) Volcanos plot of differential protein coaggregation as identified by thermal proximity coaggregation (TPCA) in combination treatment compared to DMSO. Yellow dots indicate protein pairs with significantly changed coaggregation involved in cell cycle regulation (a) and green dots indicate targets of CDK1 (b). Protein pairs labeled in B include CDC20 as an interaction partner (TUBA1A

p=0.0044; CDC27 p=0.0059; RELA p=0.0132; TUBB p=0.0129; CDK1 p=0.0152; TUBG1 p=0.0182; PBRM1 p=0.01945; CUL3 p=0.0358; HDAC1 p=0.0440). Red dashed line is p-value cut off p=0.05. c) Melt curves for p53 and TUBA1A in DMSO and combination treated cells. (p=0.0406). Tighter association of curves in DMSO treatment indicates weaker association of proteins in the complex in combination treated cells. d) Protein-protein interaction network of proteins that are changing in interaction with CDC20. String analysis shows these proteins are involved in chromosome organization, regulation of mitosis, and cytoskeleton organization, all of which can be related back to cell cycle. Node color corresponds to the complex the protein is involved in; color of lines connecting nodes corresponds to origin of protein-protein interaction annotation (black=co-expression, pink=experimentally determined, light blue=from curated database, green=textmining, purple=protein homology, red=gene fusions, dark blue=gene co-occurrence).

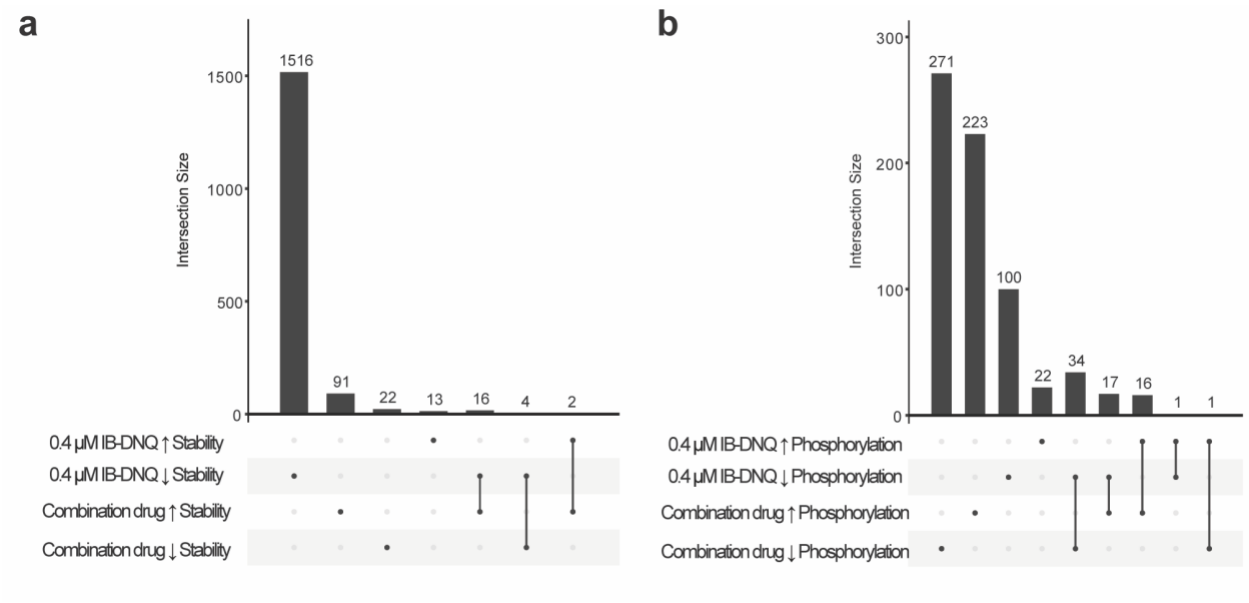

Figure 7: Comparison of protein stability changes and phosphorylation changes caused by lethal drug treatments 0.4 µM IB-DNQ or 0.1 µM IB-DNQ + 15 µM Rucaparib. a) Upset plot showing overlap between increased and decreased stability of proteins in the lethal drug treatment groups. b) Upset plot showing overlap of increased and decreased phosphorylation of peptides in the lethal drug treatment groups Intersection size is the number of unique or overlapping proteins or peptides. Single dot represents proteins or peptides that are unique to that category, and 2 dots connected with a line show where there are overlapping proteins or peptides.

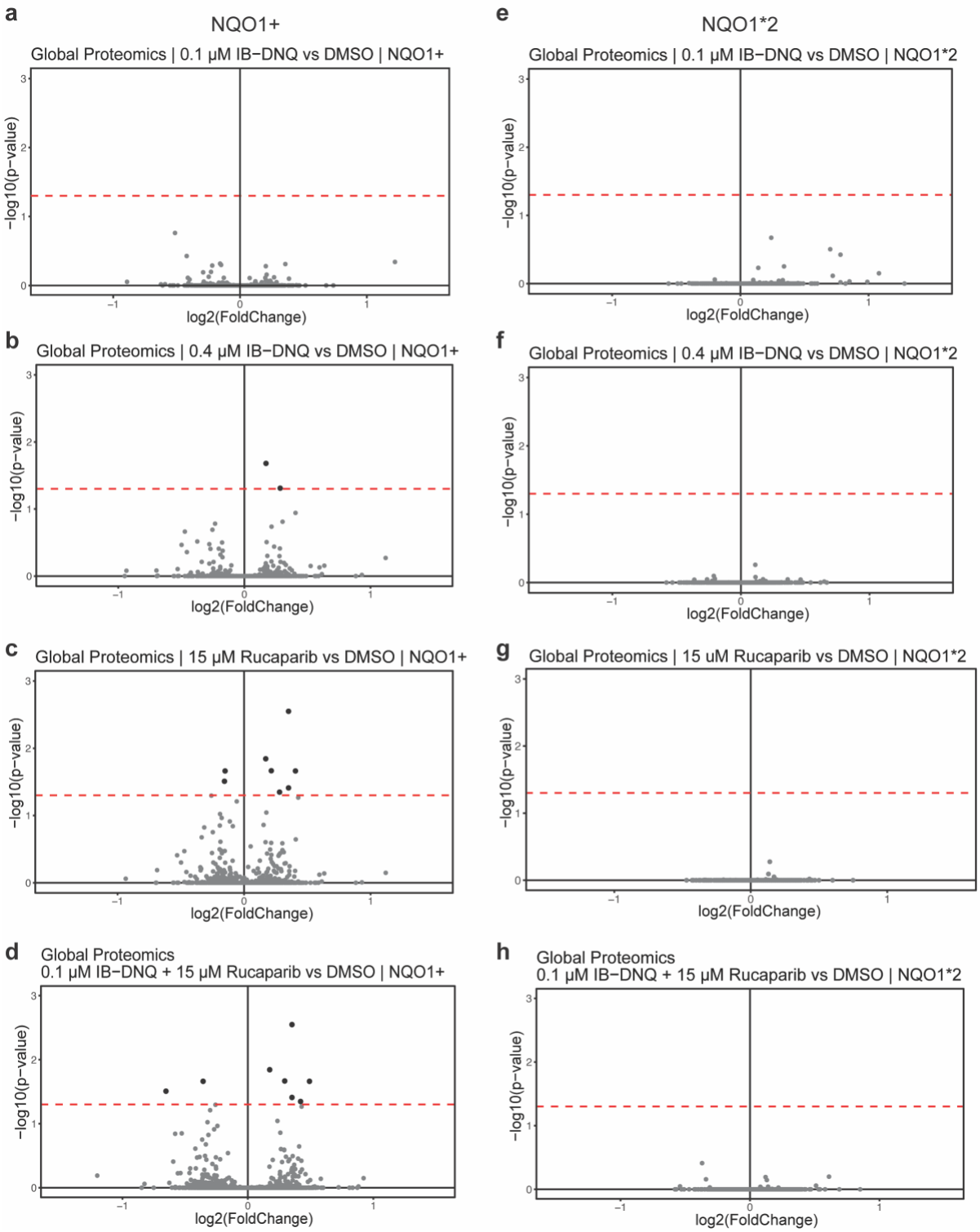
a
NQO1+
Global Proteomics | 0.1 μM IB−DNQ vs DMSO | NQO1+
b
Global Proteomics | 0.4 μM IB−DNQ vs DMSO | NQO1+
c
Global Proteomics | 15 μM Rucaparib vs DMSO | NQO1+
d
Global Proteomics
0.1 μM IB−DNQ + 15 μM Rucaparib vs DMSO | NQO1+
e
NQO1*2
Global Proteomics | 0.1 μM IB−DNQ vs DMSO | NQO1*2
f
Global Proteomics | 0.4 μM IB−DNQ vs DMSO | NQO1*2
g
Global Proteomics | 15 uM Rucaparib vs DMSO | NQO1*2
h
Global Proteomics
0.1 μM IB−DNQ + 15 μM Rucaparib vs DMSO | NQO1*2
−log10(p−value)
log2(FoldChange)

Supplementary Figure 1: Global proteomics of NQO1+ (a-d) and NQO1*2 (e-h) MDA-MB-231 cells treated with 0.1 µM IB-DNQ (a,e), 0.4 µM IB-DNQ (b,f), 15 µM Rucaparib (c,g), or combination treatment (d,h). Red dashed line is p-value cut off p=0.05.

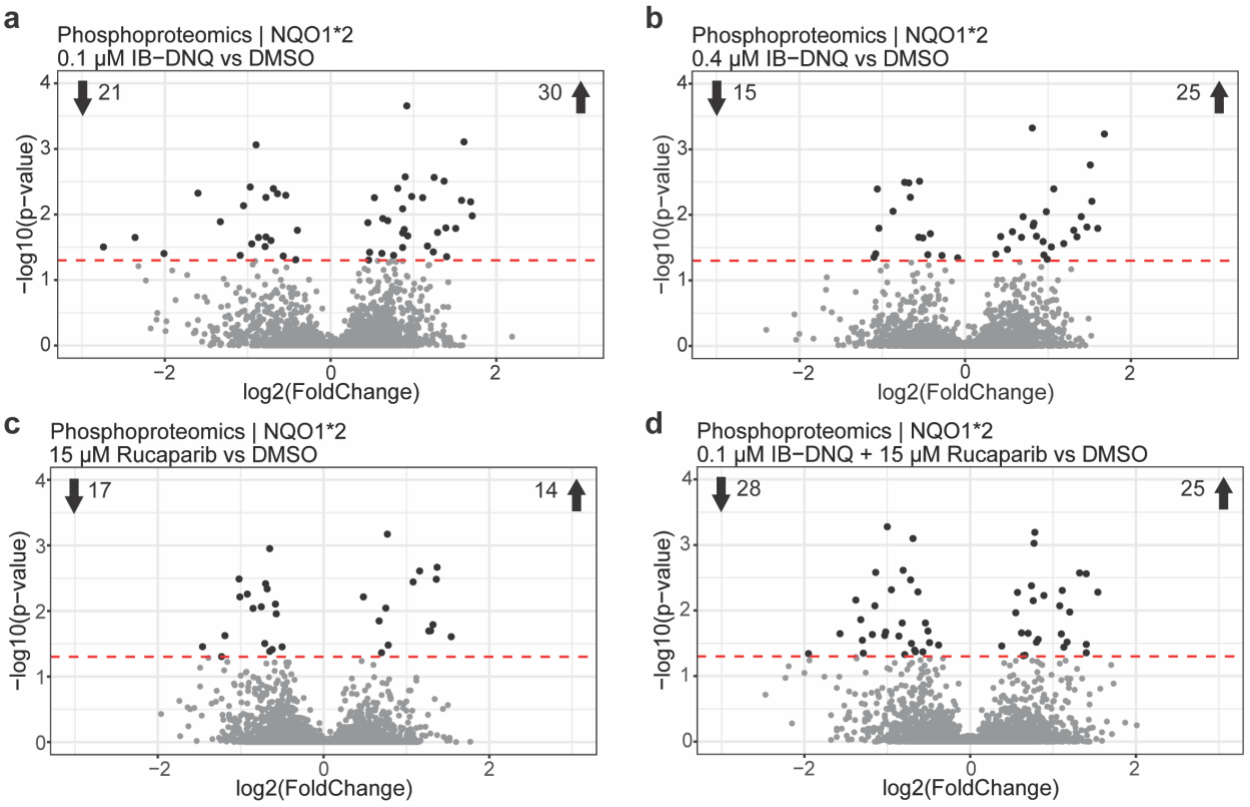

Supplementary Figure 2: Phosphoproteomics of NQO1*2 MDA-MB-231 cells. Volcano plots show differential phosphorylation of peptide groups in drug treated NQO1*2 cells compared to DMSO treated cells. Red dashed line is p-value cut off p=0.05.

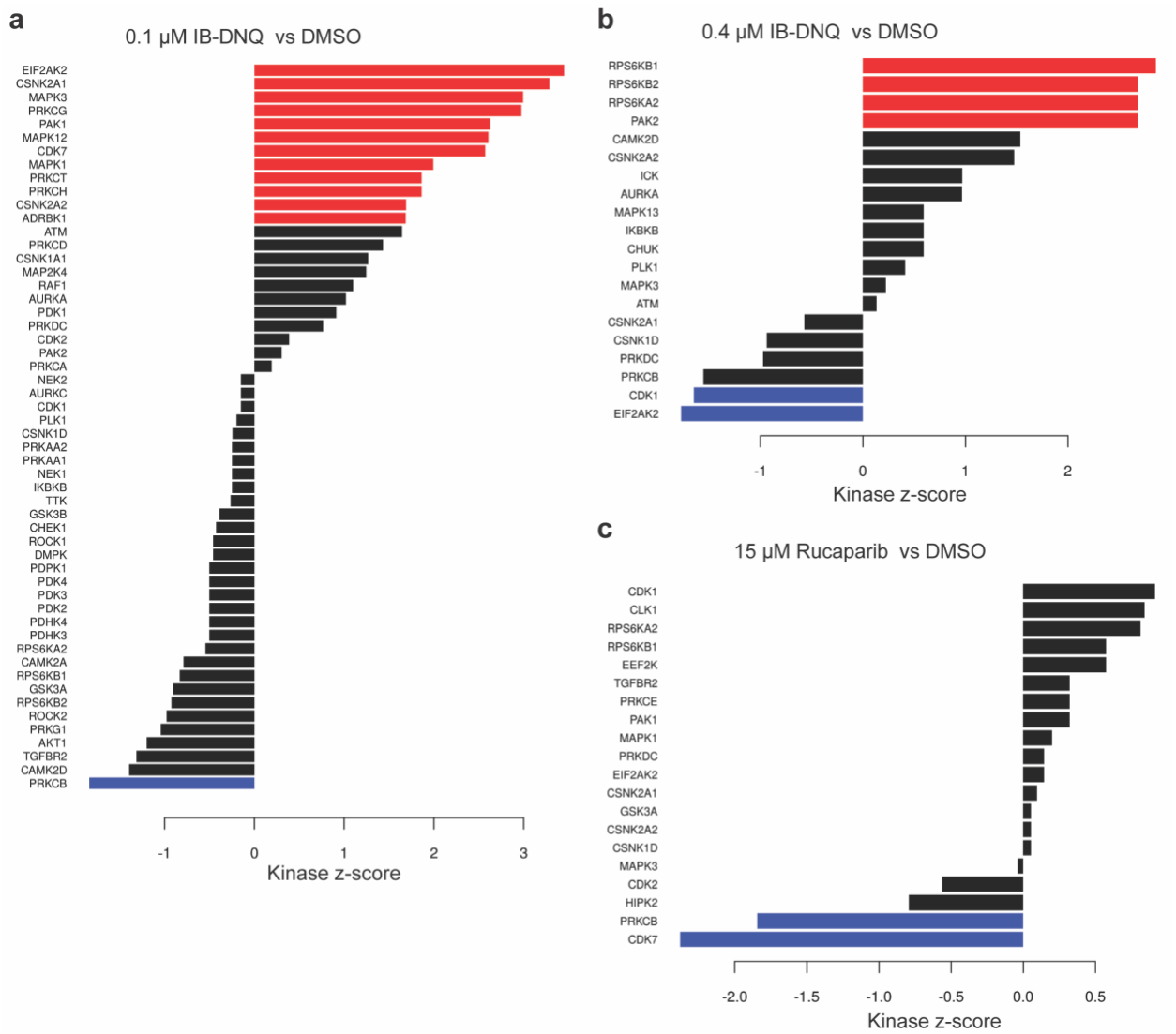

Supplementary Figure 3: Kinase substrate enrichment analysis (KSEA) of NQO1+ single agent treated cells compared to DMSO. KSEA bar plots for 0.1 μM IB-DNQ (a), 0.4 μM IB-DNQ (b), and 15 μM Rucaparib (c). Red bars indicate kinases with significantly increased inferred activity ($p<0.05$), and blue bars indicate kinases with significantly decreased inferred activity. Black bars show kinases with differential inferred kinase activity but are not statistically significant.

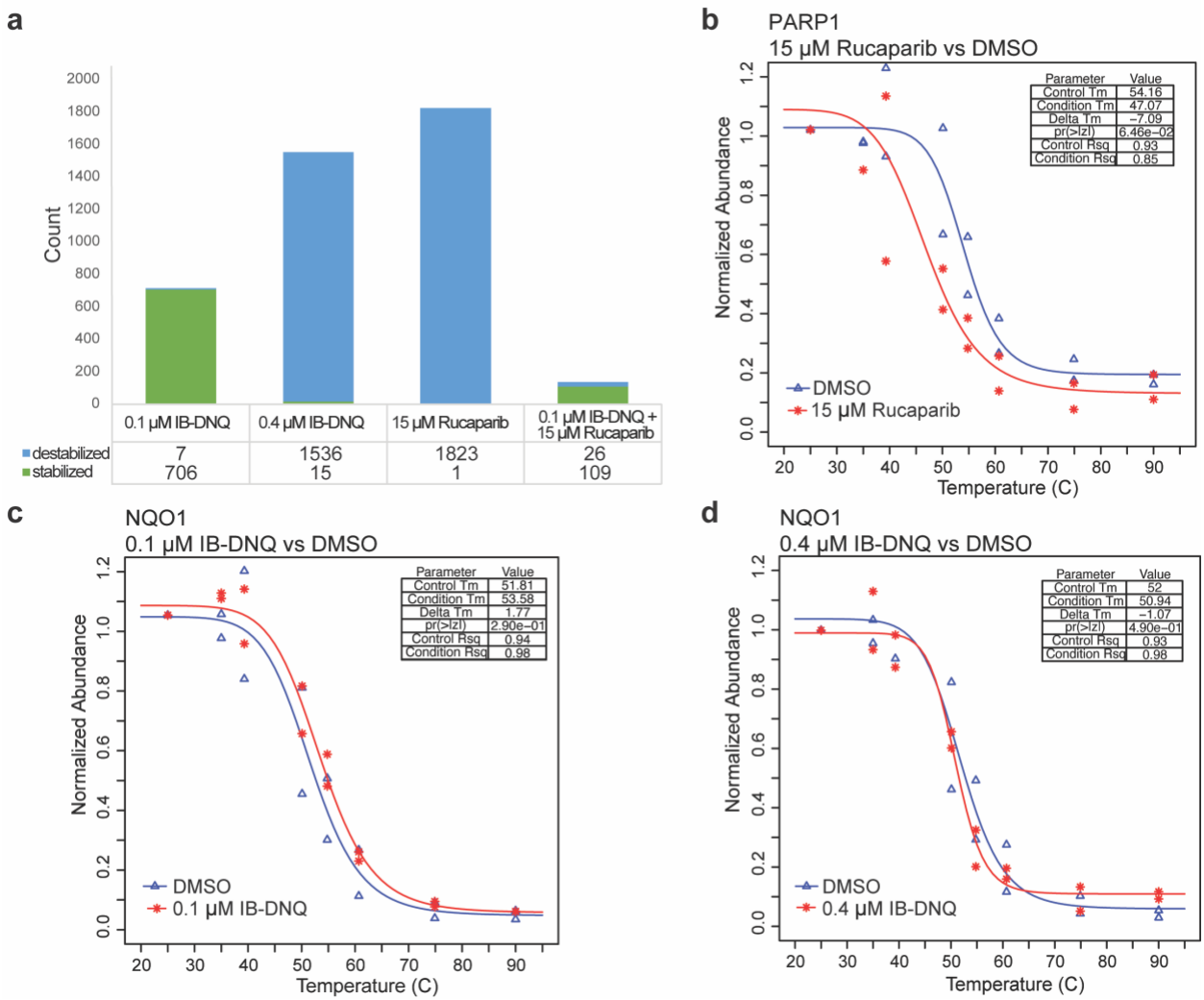

Supplementary Figure 4: Thermal proteome profiling. a) Summary of stabilized and destabilized proteins in each condition compared to DMSO in NQO1+ cells. b) Melt curves for PARP1 (Rucaparib target) from 15 µM Rucaparib compared to DMSO treated NQO1+ cells. c,d) Melt curves for NQO1 (IB-DNQ target) from 0.1 µM IB-DNQ treated NQO1+ cells (c) and 0.4 µM IB-DNQ treated NQO1+ cells (d) compared to DMSO.

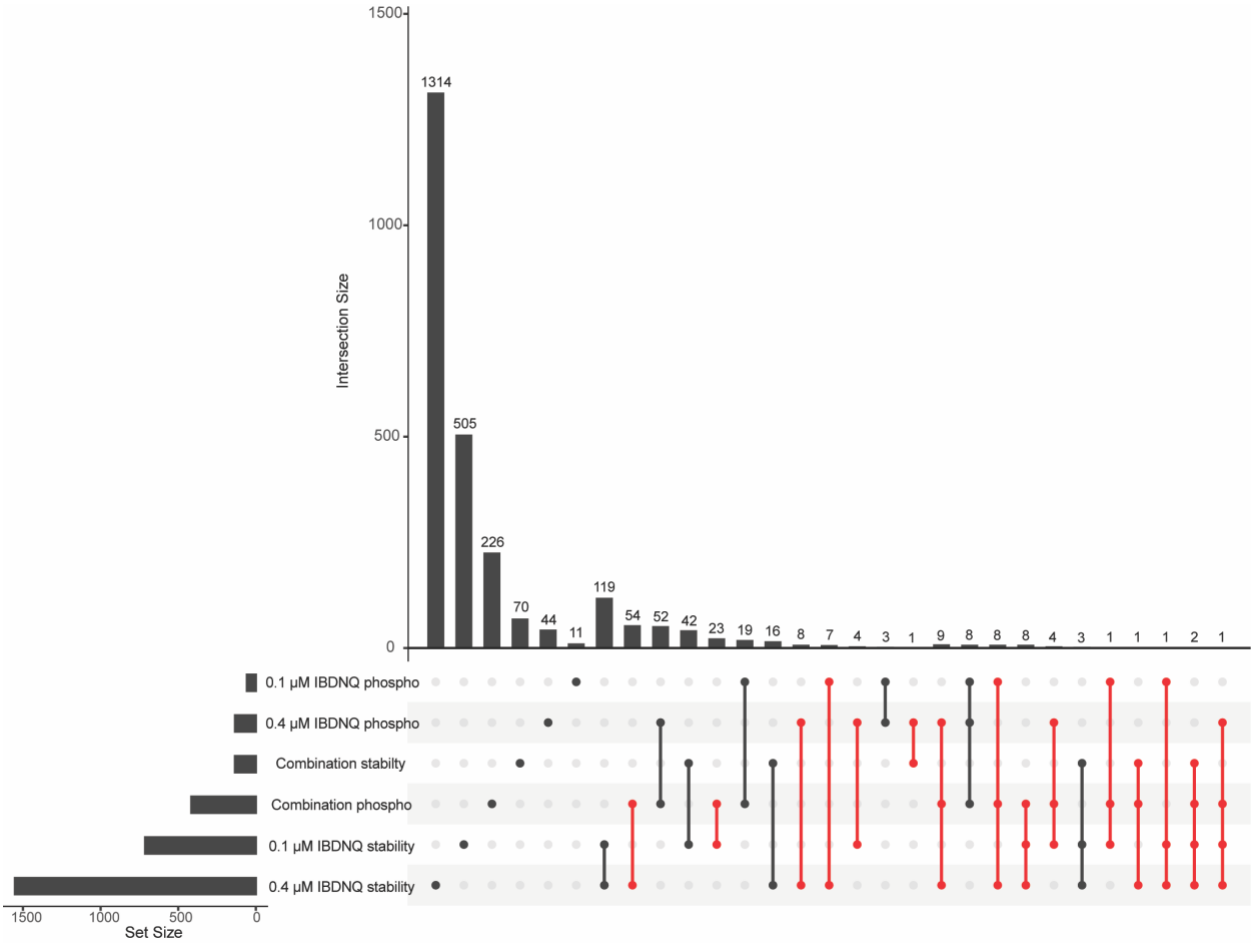

Supplementary Figure 5: Comparison of proteins with phosphorylation and thermal stability changes in each of the IB-DNQ treatment groups (0.1 µM, 0.4 µM, and combination treatment). Upset plot showing overlap of phosphorylation and thermal stability changes. Intersection size is the number of unique or overlapping proteins or peptides. Single dot represents proteins or peptides that are unique to that category, and 2 or more dots connected with a line show where there are overlapping proteins. Red connections show overlaps of stability and phosphorylation changes. Set size shows the total number of significant changes in each category.

REFERENCES

1. Yin L, Duan JJ, Bian XW, Yu SC. Triple-negative breast cancer molecular subtyping and treatment progress. Breast Cancer Res BCR. 2020 Jun 9;22(1):61.

2. Almansour NM. Triple-Negative Breast Cancer: A Brief Review About Epidemiology, Risk Factors, Signaling Pathways, Treatment and Role of Artificial Intelligence. Front Mol Biosci. 2022 Jan 25;9:836417.

3. Howard FM, Olopade OI. Epidemiology of Triple-Negative Breast Cancer: A Review. Cancer J Sudbury Mass. 2021 Feb 1;27(1):8–16.

4. Brenton JD, Carey LA, Ahmed AA, Caldas C. Molecular Classification and Molecular Forecasting of Breast Cancer: Ready for Clinical Application? J Clin Oncol. 2005 Oct 10;23(29):7350–60.

5. Foulkes WD, Smith IE, Reis-Filho JS. Triple-Negative Breast Cancer. N Engl J Med. 2010 Nov 11;363(20):1938–48.

6. Motea EA, Huang X, Singh N, Kilgore J, Williams N, Xie XJ, et al. NQO1-dependent, tumor-selective radiosensitization of non-small cell lung cancers. Clin Cancer Res Off J Am Assoc Cancer Res. 2019 Apr 15;25(8):2601–9.

7. Huang X, Dong Y, Bey EA, Kilgore JA, Bair JS, Li LS, et al. An NQO1 Substrate with Potent Antitumor Activity That Selectively Kills by PARP1-Induced Programmed Necrosis. Cancer Res. 2012 Jun 14;72(12):3038–47.

8. Gerber DE, Beg MS, Fattah F, Frankel AE, Fatunde O, Arriaga Y, et al. Phase 1 study of ARQ 761, a β-lapachone analogue that promotes NQO1-mediated programmed cancer cell necrosis. Br J Cancer. 2018 Oct;119(8):928–36.

9. Parkinson EI, Bair JS, Cismesia M, Hergenrother PJ. Efficient NQO1 substrates are potent and selective anticancer agents. ACS Chem Biol. 2013 Oct 18;8(10):2173–83.

10. Wettasinghe AP, Singh N, Starcher CL, DiTusa CC, Ishak-Boushaki Z, Kahanda D, et al. Detecting Attomolar DNA-Damaging Anticancer Drug Activity in Cell Lysates with Electrochemical DNA Devices. ACS Sens. 2021 Jul 23;6(7):2622–9.

11. Huang X, Motea EA, Moore ZR, Yao J, Dong Y, Chakrabarti G, et al. Leveraging an NQO1 Bioactivatable Drug for Tumor-Selective Use of Poly(ADP-ribose) Polymerase Inhibitors. Cancer Cell. 2016 Dec;30(6):940–52.

12. Bey EA, Bentle MS, Reinicke KE, Dong Y, Yang CR, Girard L, et al. An NQO1- and PARP-1-mediated cell death pathway induced in non-small-cell lung cancer cells by β-lapachone. Proc Natl Acad Sci. 2007 Jul 10;104(28):11832–7.

13. Chakrabarti G, Silvers MA, Ilcheva M, Liu Y, Moore ZR, Luo X, et al. Tumor-selective use of DNA base excision repair inhibition in pancreatic cancer using the NQO1 bioactivatable drug, β-lapachone. Sci Rep. 2015 Nov 25;5:17066.

14. Siegel D, Ross D. Immunodetection of NAD(P)H:quinone oxidoreductase 1 (NQO1) in human tissues. Free Radic Biol Med. 2000 Aug;29(3–4):246–53.

15. Begleiter A, Fourie J. Induction of NQO1 in cancer cells. Methods Enzymol. 2004;382:320–51.

16. Deller S, Macheroux P, Sollner S. Flavin-dependent quinone reductases. Cell Mol Life Sci. 2008 Jan 1;65(1):141–60.

17. Pink JJ, Planchon SM, Tagliarino C, Varnes ME, Siegel D, Boothman DA. NAD(P)H:Quinone oxidoreductase activity is the principal determinant of beta-lapachone cytotoxicity. J Biol Chem. 2000 Feb 25;275(8):5416–24.

18. Finkel T, Holbrook NJ. Oxidants, oxidative stress and the biology of ageing. Nature. 2000;408(6809):239–47.

19. Wang M, Chen S, Ao D. Targeting DNA repair pathway in cancer: Mechanisms and clinical application. MedComm. 2021;2(4):654–91.

20. Torgovnick A, Schumacher B. DNA repair mechanisms in cancer development and therapy. Front Genet. 2015 Apr 23;6:157.

21. Rose M, Burgess JT, O'Byrne K, Richard DJ, Bolderson E. PARP Inhibitors: Clinical Relevance, Mechanisms of Action and Tumor Resistance. Front Cell Dev Biol. 2020 Sep 9;8:564601.

22. Dantzer F, De La Rubia G, Ménissier-De Murcia J, Hostomsky Z, De Murcia G, Schreiber V. Base excision repair is impaired in mammalian cells lacking poly(ADP-ribose) polymerase-1. Biochemistry. 2000;39(25):7559–69.

23. Wang M, Wu W, Wu W, Rosidi B, Zhang L, Wang H, et al. PARP-1 and Ku compete for repair of DNA double strand breaks by distinct NHEJ pathways. Nucleic Acids Res. 2006 Nov 1;34(21):6170–82.

24. Helleday T, Petermann E, Lundin C, Hodgson B, Sharma RA. DNA repair pathways as targets for cancer therapy. Nat Rev Cancer. 2008 Mar;8(3):193–204.

25. Lee J m., Ledermann JA, Kohn EC. PARP Inhibitors for BRCA1/2 mutation-associated and BRCA-like malignancies. Ann Oncol. 2014 Jan 1;25(1):32–40.

26. Wiredja DD, Koyutürk M, Chance MR. The KSEA App: a web-based tool for kinase activity inference from quantitative phosphoproteomics. Bioinformatics. 2017 Nov 1;33(21):3489–91.

27. Casado P, Rodriguez-Prados JC, Cosulich SC, Guichard S, Vanhaesebroeck B, Joel S, et al. Kinase-substrate enrichment analysis provides insights into the heterogeneity of signaling pathway activation in leukemia cells. Sci Signal. 2013 Mar 26;6(268):rs6.

28. Hornbeck PV, Zhang B, Murray B, Kornhauser JM, Latham V, Skrzypek E. PhosphoSitePlus, 2014: mutations, PTMs and recalibrations. Nucleic Acids Res. 2015 Jan 28;43(D1):D512–20.

29. Horn H, Schoof EM, Kim J, Robin X, Miller ML, Diella F, et al. KinomeXplorer: an integrated platform for kinome biology studies. Nat Methods. 2014 Jun;11(6):603–4.

30. Linding R, Jensen LJ, Ostheimer GJ, van Vugt MATM, Jørgensen C, Miron IM, et al. Systematic discovery of in vivo phosphorylation networks. Cell. 2007 Jun 29;129(7):1415–26.

31. Linding R, Jensen LJ, Pasculescu A, Olhovsky M, Colwill K, Bork P, et al. NetworKIN: a resource for exploring cellular phosphorylation networks. Nucleic Acids Res. 2008 Jan;36(Database issue):D695-699.

32. Matthews HK, Bertoli C, de Bruin RAM. Cell cycle control in cancer. Nat Rev Mol Cell Biol. 2022 Jan;23(1):74–88.

33. Fang Y, Zhang X. Targeting NEK2 as a promising therapeutic approach for cancer treatment. Cell Cycle. 2016 Mar 28;15(7):895–907.

34. Sasai K, Katayama H, Stenoien DL, Fujii S, Honda R, Kimura M, et al. Aurora-C kinase is a novel chromosomal passenger protein that can complement Aurora-B kinase function in mitotic cells. Cell Motil Cytoskeleton. 2004 Dec;59(4):249–63.

35. Bignone PA, Lee KY, Liu Y, Emilion G, Finch J, Soosay AER, et al. RPS6KA2, a putative tumour suppressor gene at 6q27 in sporadic epithelial ovarian cancer. Oncogene. 2007 Feb 1;26(5):683–700.

36. Mitsushima M, Toyoshima F, Nishida E. Dual role of Cdc42 in spindle orientation control of adherent cells. Mol Cell Biol. 2009 May;29(10):2816–27.

37. Archambault V, Lépine G, Kachaner D. Understanding the Polo Kinase machine. Oncogene. 2015 Sep;34(37):4799–807.

38. Reinhardt HC, Yaffe MB. Kinases that Control the Cell Cycle in Response to DNA Damage: Chk1, Chk2, and MK2. Curr Opin Cell Biol. 2009 Apr;21(2):245–55.

39. Tan CSH, Go KD, Bisteau X, Dai L, Yong CH, Prabhu N, et al. Thermal proximity coaggregation for system-wide profiling of protein complex dynamics in cells. Science. 2018 Mar 9;359(6380):1170–7.

40. Peck Justice SA, Barron MP, Qi GD, Wijeratne HRS, Victorino JF, Simpson ER, et al. Mutant thermal proteome profiling for characterization of missense protein variants and their associated phenotypes within the proteome. J Biol Chem. 2020 Nov;295(48):16219–38.

41. Huang JX, Lee G, Cavanaugh KE, Chang JW, Gardel ML, Moellering RE. High throughput discovery of functional protein modifications by Hotspot Thermal Profiling. Nat Methods. 2019 Sep;16(9):894–901.

42. Becher I, Andrés-Pons A, Romanov N, Stein F, Schramm M, Baudin F, et al. Pervasive Protein Thermal Stability Variation during the Cell Cycle. Cell. 2018 May 31;173(6):1495-1507.e18.

43. Martinez Molina D, Jafari R, Ignatushchenko M, Seki T, Larsson EA, Dan C, et al. Monitoring drug target engagement in cells and tissues using the cellular thermal shift assay. Science. 2013 Jul 5;341(6141):84–7.

44. McCracken NA, Peck Justice SA, Wijeratne AB, Mosley AL. Inflect: Optimizing Computational Workflows for Thermal Proteome Profiling Data Analysis. J Proteome Res. 2021 Apr 2;20(4):1874–88.

45. McCracken NA, Liu H, Runnebohm AM, Wijeratne HRS, Wijeratne AB, Staschke KA, et al. Obtaining Functional Proteomics Insights From Thermal Proteome Profiling Through Optimized Melt Shift Calculation and Statistical Analysis With InflectSSP. Mol Cell Proteomics MCP. 2023 Aug 9;22(9):100630.

46. Mah LJ, El-Osta A, Karagiannis TC. γH2AX: a sensitive molecular marker of DNA damage and repair. Leukemia. 2010 Apr;24(4):679–86.

47. Podhorecka M, Skladanowski A, Bozko P. H2AX Phosphorylation: Its Role in DNA Damage Response and Cancer Therapy. J Nucleic Acids. 2010 Aug 3;2010:920161.

48. Burma S, Chen BP, Murphy M, Kurimasa A, Chen DJ. ATM phosphorylates histone H2AX in response to DNA double-strand breaks. J Biol Chem. 2001 Nov 9;276(45):42462–7.

49. Ward IM, Chen J. Histone H2AX is phosphorylated in an ATR-dependent manner in response to replicational stress. J Biol Chem. 2001 Dec 21;276(51):47759–62.

50. Xiao A, Li H, Shechter D, Ahn SH, Fabrizio LA, Erdjument-Bromage H, et al. WSTF regulates the function of H2A.X via a novel tyrosine kinase activity. Nature. 2009 Jan 1;457(7225):57–62.

51. Cook PJ, Ju BG, Telese F, Wang X, Glass CK, Rosenfeld MG. Tyrosine Dephosphorylation of H2AX Modulates Apoptosis and Survival Decisions. Nature. 2009 Apr 2;458(7238):591–6.

52. Kurzawa N, Mateus A, Savitski MM. Rtpca: an R package for differential thermal proximity coaggregation analysis. Luigi Martelli P, editor. Bioinformatics. 2021 Apr 20;37(3):431–3.

53. Mathur R, Roberts CWM. SWI/SNF (BAF) Complexes: Guardians of the Epigenome. Annu Rev Cancer Biol. 2018;2(1):413–27.

54. Tarapore P, Horn HF, Tokuyama Y, Fukasawa K. Direct regulation of the centrosome duplication cycle by the p53-p21Waf1/Cip1 pathway. Oncogene. 2001 May;20(25):3173–84.

55. Giannakakou P, Sackett DL, Ward Y, Webster KR, Blagosklonny MV, Fojo T. p53 is associated with cellular microtubules and is transported to the nucleus by dynein. Nat Cell Biol. 2000 Oct;2(10):709–17.

56. Viktorsson K, Rieckmann T, Fleischmann M, Diefenhardt M, Hehlgans S, Rödel F. Advances in molecular targeted therapies to increase efficacy of (chemo)radiation therapy. Strahlenther Onkol. 2023;199(12):1091–109.

57. Ribeiro-Silva C, Vermeulen W, Lans H. SWI/SNF: Complex complexes in genome stability and cancer. DNA Repair. 2019 May;77:87–95.

58. Harrod A, Lane KA, Downs JA. The role of the SWI/SNF chromatin remodelling complex in the response to DNA double strand breaks. DNA Repair. 2020 Sep;93:102919.

59. Lans H, Marteijn JA, Vermeulen W. ATP-dependent chromatin remodeling in the DNA-damage response. Epigenetics Chromatin. 2012 Jan 30;5(1):4.

60. Davó-Martínez C, Helfricht A, Ribeiro-Silva C, Raams A, Tresini M, Uruci S, et al. Different SWI/SNF complexes coordinately promote R-loop- and RAD52-dependent transcription-coupled homologous recombination. Nucleic Acids Res. 2023 Jul 20;51(17):9055–74.

61. Contadini C, Monteonofrio L, Virdia I, Prodosmo A, Valente D, Chessa L, et al. p53 mitotic centrosome localization preserves centrosome integrity and works as sensor for the mitotic surveillance pathway. Cell Death Dis. 2019 Nov 7;10(11):1–16.

62. Tsitsiridis G, Steinkamp R, Giurgiu M, Brauner B, Fobo G, Frishman G, et al. CORUM: the comprehensive resource of mammalian protein complexes–2022. Nucleic Acids Res. 2023 Jan 6;51(D1):D539–45.

63. Ruepp A, Brauner B, Dunger-Kaltenbach I, Frishman G, Montrone C, Stransky M, et al. CORUM: the comprehensive resource of mammalian protein complexes. Nucleic Acids Res. 2008 Jan 1;36(suppl_1):D646–50.

64. Stark C, Breitkreutz BJ, Reguly T, Boucher L, Breitkreutz A, Tyers M. BioGRID: a general repository for interaction datasets. Nucleic Acids Res. 2006 Jan 1;34(suppl_1):D535–9.

65. Wickham H. ggplot2: Elegant Graphics for Data Analysis [Internet]. New York, NY: Springer; 2009 [cited 2023 Jun 6]. Available from: https://link.springer.com/10.1007/978-0-387-98141-3

66. Conway JR, Lex A, Gehlenborg N. UpSetR: an R package for the visualization of intersecting sets and their properties. Bioinformatics. 2017 Sep 15;33(18):2938–40.

67. Silvers MA, Deja S, Singh N, Egnatchik RA, Sudderth J, Luo X, et al. The NQO1 bioactivatable drug, β-lapachone, alters the redox state of NQO1+ pancreatic cancer cells, causing perturbation in central carbon metabolism. J Biol Chem. 2017 Nov 3;292(44):18203–16.